12-2015

Ion Irradiation-induced Microstructural Change in SiC

Chien-Hung Chen
University of Tennessee - Knoxville, cchen30@vols.utk.edu

To the Graduate Council:

I am submitting herewith a dissertation written by Chien-Hung Chen entitled "Ion Irradiation-induced Microstructural Change in SiC." I have examined the final electronic copy of this dissertation for form and content and recommend that it be accepted in partial fulfillment of the requirements for the degree of Doctor of Philosophy, with a major in Materials Science and Engineering.

William J. Weber, Major Professor

We have read this dissertation and recommend its acceptance:

Yanwen Zhang, Gerd Duscher, Maik K. Lang

Accepted for the Council:

Carolyn R. Hodges

Vice Provost and Dean of the Graduate School

(Original signatures are on file with official student records.)

Ion Irradiation-induced Microstructural Change in SiC

A Dissertation Presented for the
Doctor of Philosophy
Degree
The University of Tennessee, Knoxville

Chien-Hung Chen
December 2015

ACKNOWLEDGEMENTS

I would like to express my sincere gratitude to my advisors Prof. Weber and Prof. Zhang for their continuous support of my Ph.D study and related research, as well as for their patience, motivation, and immense knowledge. Their guidance helped me throughout the time of research and writing of this thesis. I could not have imagined having better advisors and mentors for my Ph.D study.

Besides my advisors, I would like to thank my thesis committee members, Prof. Duscher and Prof. Lang, for their insightful comments and encouragement, but also for the hard questions that inspired me to broaden my research perspectives.

I would also like to thank my lab-mates for all the discussions and cooperation over the last four years. Also, I thank my friends in the following institutions: Oak Ridge National Laboratory, Los Alamos National Laboratory and Argonne National Laboratory. In particular, I am grateful to Prof. Kai and Prof. Chen for inspiring me to pursue research when I was in college.

Last but not the least, I would like to thank my family members and my girlfriend, for supporting me spiritually in my life.

ABSTRACT

The high temperature radiation resistance of nuclear materials has become a key issue in developing future nuclear reactors. Because of its mechanical stability under high-energy neutron irradiation and high temperature, silicon carbide (SiC) has great potential as a structural material in advanced nuclear energy systems.

A newly developed nano-engineered (NE) 3C SiC with a nano-layered stacking fault (SFs) structure has been recently considered as a prospective choice due to enhanced point defect annihilation between layer-type structures, leading to outstanding radiation durability.

The objective of this project was to advance the understanding of gas bubble formation mechanisms under irradiation conditions in SiC. In this work, microstructural evolution induced by helium implantation and ion irradiation was investigated in single crystal and NE SiC. Elastic recoil detection analysis confirmed that the as-implanted helium depth profile did not change under irradiation to 30 dpa at 700 °C. Helium bubbles were found in NE SiC after heavy ion irradiation at a lower temperature than in previous literature results. These results expand the current understanding of helium migration mechanism of NE SiC under high temperature irradiation environment.

No obvious bubble growth was observed after ion irradiation at 700 °C, suggesting a long helium bubble incubation process under continued irradiation at this temperature and dose. As determined by electron energy loss spectroscopy measurements, only 1 % of the implanted helium atoms are trapped in bubbles. Helium redistribution and release was observed in the TEM samples under *in-situ* irradiation at 800 °C. *In-situ* TEM analysis revealed that the nano-layered SF structure is radiation tolerant below a dose of about 15 dpa at 800 °C, but continued irradiation to 20 dpa under these *in-situ* conditions leads to

loss of the stacking fault structure, which may be a manifestation of irradiating thin TEM foils. The irradiation stability of the SF structure under bulk irradiation remains unknown. This stacking fault structure is critical since it suppresses the formation of dislocation loops normally observed under these irradiation conditions. Systematic studies towards understanding the role of defect migration under irradiation on the evolution of helium bubbles in NE SiC were performed.

Keywords

SiC, Irradiation, Helium Bubble, TEM/STEM, EELS, *In-situ*, ERDA

TABLE OF CONTENTS

LIST OF TABLES

LIST OF FIGURES

Chapter 1. Introduction

1.1. Brief history of Fusion reactor development

Due to the limitation of fossil fuel, scientists advocate the development of alternative energy, sources that bring no undesirable consequences inherent in fossil fuel use, especially in global warming. Nuclear energy, compared to other alternative energies like solar, wind and geothermal energy, provides a sustainable energy source with relative low costs. However, there is an ongoing debate about nuclear fission power usage. Opponents claim that radioactive waste and potential nuclear power plant accidents may threaten people and the environment for several generations. After nuclear accidents during the last few decades (Three Mile Island, Chernobyl and Fukushima), scientists have been urged to find alternative energy sources and accelerate the development of fusion nuclear power plants.

The advantages of fusion nuclear power plant are:
1. Low cost and unlimited fuels (tritium can be bred in the reactor and deuterium can be distilled from seawater)
2. Easy to shut down (no chain reaction)
3. Significantly less long-term radioactive waste (most of the wastes are only radioactive for less than 100 years.)

In nuclear physics, fusion means the collision of two or more atomic nuclei to form a new atomic nucleus. Energetic particle emissions occur during the fusion process. It's also well known that the fusion reaction is the main reaction that powers the sun. However, activating the fusion nuclear reaction requires overcoming the repulsive Coulomb force from positively charged subnuclear particles in the atomic nuclei. It can be accomplished by providing extremely high

kinetic energy to each atom, including acceleration and heating. Although there are different ways to achieve the fusion reaction, at such a high-energy state, all the electrons from the atoms are stripped away, leaving behind the bear atomic nucleus or ion. These separated ions and electron clouds are the hot plasma in a fusion device. At this state, no solid material container can withstand such extreme temperatures. Due to the instability of plasma confinement, the fusion power reactor is still under development. The most popular fusion approaches are inertial confinement and magnetic confinement.

Inertial confinement fusion

Fusion fuels (mixture of deuterium and tritium) are embedded in fuel pellets. Energy will be first delivered through high-energy laser beams to the outer layer of the fusion target. With such a high-energy flux, the temperature of pellets will be driven to the ignition point for fusion (over 100 million degrees Celsius) in 10^{-11} to 10^{-9} seconds. In this short time interval, atomic nuclei will fuse before they have time to move away from each other. Scientists from the National Ignition Facility (NIF) (i.e., Lawrence Livermore National Laboratory (LLNL), California, USA) have achieved a "fuel gain" of greater than one in 2014. They reported that 10 kJ of energy delivered to the fuel from a single laser shot led to 14 kJ and 17 kJ of fusion energy production in two different experiments [5].

Magnetic confinement fusion

In this approach, the magnetic field is employed to confine the hot fusion fuels (in the form of a plasma) out of contact with the container (first wall). Using the magnetic field, the moving plasma with charged particles floats in helical or circular paths. The most well-known Magnetic confinement fusion reactor is the Tokamak reactor. During the mid-1950s, Tokamak reactors were first invented by Soviet physicists Igor Tamm and Andrei Sakharov. Tokamak is one of several

types of magnetic confinement devices, with a unique doughnut-shaped magnetic field to confine all high velocity positively and negatively charged ions and electrons, as shown in Fig. 1-1(a) and 1-1(b). In the fusion reaction, the ratio of fusion power to input power is a key indicator that determines whether this process can produce more energy than it consumes. Previously, the output/input energy ratio of 1.25 has been achieved on the JT-60 fusion reactor (with the D–T reaction) in Japan. Although a self-sustaining nuclear fusion reaction would need an output/input energy ratio larger than 5, the development of a commercial fusion power plant for future generations is an expectation.

Possible fusion reactions in reactor

Generally speaking, there are 3 key fusion reactions that can be used in a fusion power plant:

1. ${}_1^2D + {}_1^3T \rightarrow {}_2^4He + n \quad Q = 17.6\ MeV$
2. ${}_1^2D + {}_1^2D \rightarrow {}_1^3T + {}_1^1H \quad Q = 4\ MeV\ (50\%)$
   ${}_1^2D + {}_1^2D \rightarrow {}_2^3He + n \quad Q = 3.25\ MeV\ (50\%)$
3. ${}_1^2D + {}_2^3He \rightarrow {}_2^4He + {}_1^1H \quad Q = 18.2\ MeV$

The relation of fusion reactivity and plasma temperature is illustrated in Fig. 1-2 [6]. It's clear that for the D-T reaction, higher reactivity can be achieved at lower temperatures. That is the reason scientists are mainly focusing on developing the D-T fusion reactor (i.e., for the D-T reaction, when reactivity is larger than 1, the ion temperature is higher than 10 keV, which is equal to 100 million degrees Kelvin.)

Based on Lawson's criterion, to keep a self-sustain fusion status, the plasma needs to be maintained above the critical ignition temperature. Also, the plasma must be sustained at a certain temperature for a minimum length of time in order

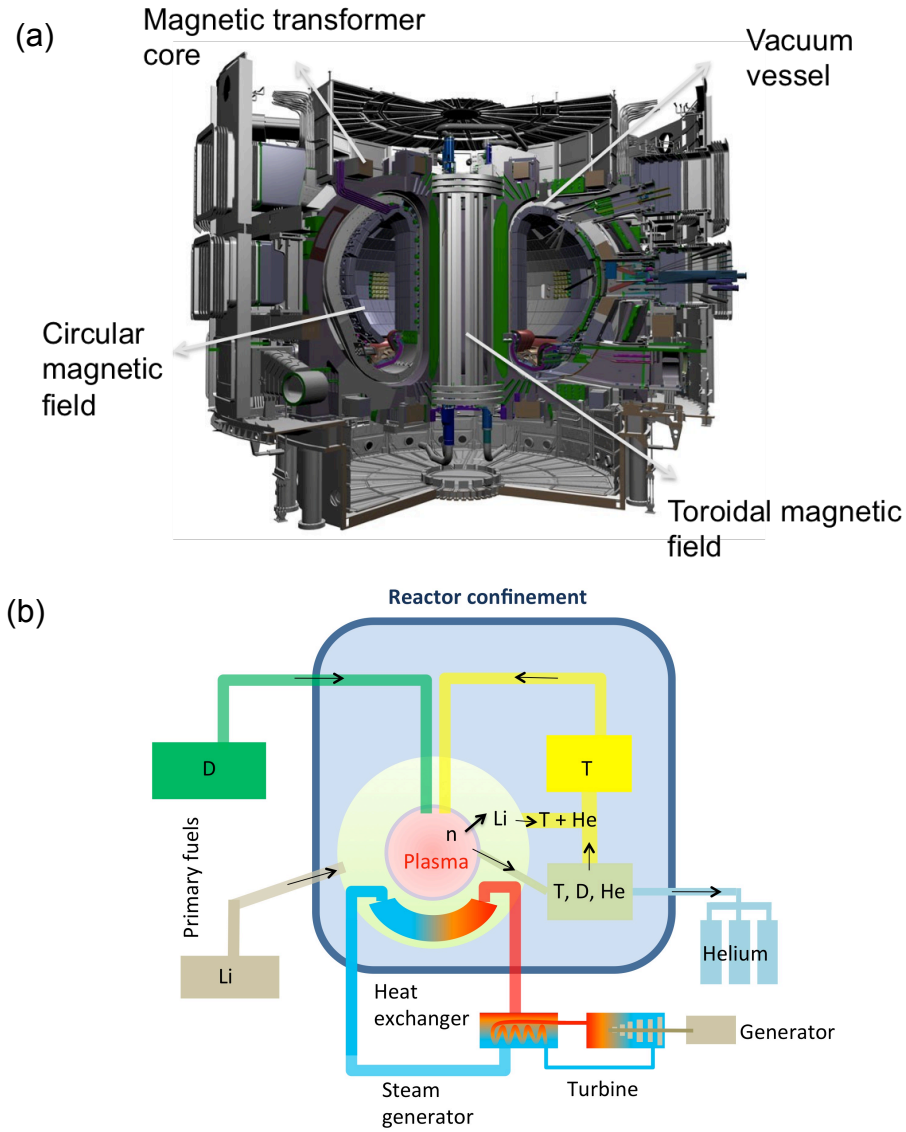

Fig. 1-1 (a) A Tokamak design of fusion reactor and (b) Tokamak reactor schematic.

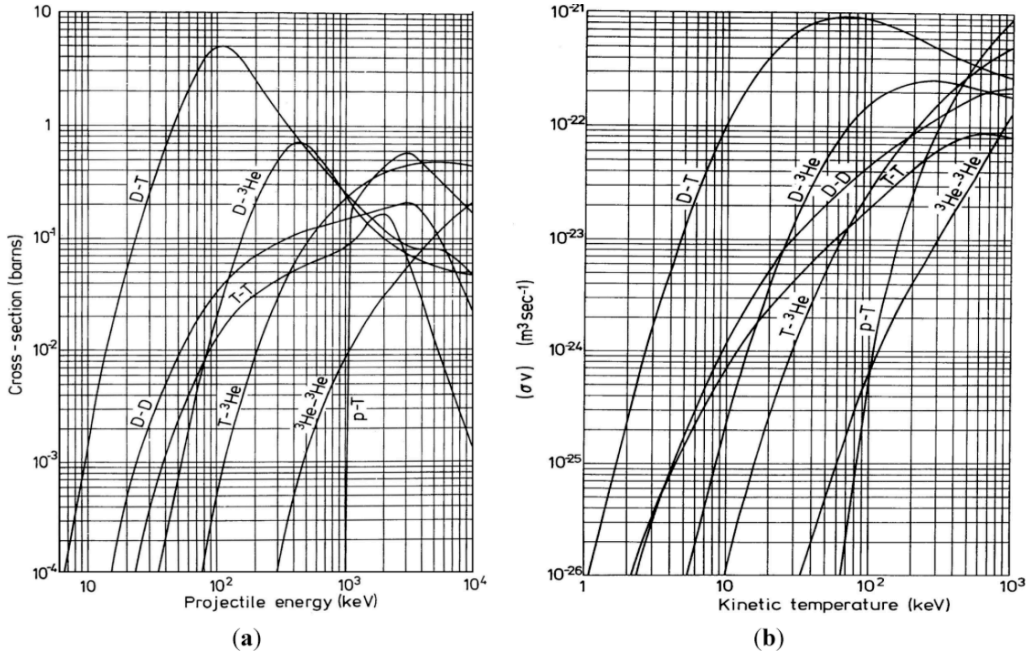

Fig. 1-2 Reactivity of different types of fusion reactions. (a) relation between the nuclear fusion cross-section and projectile energy and (b) relation between the average of the fusion cross-section σ over the relative velocities v and plasma temperature.

to yield more energy from fusion than what has been invested for heating the plasma. As illustrated in Fig. 1-3 [7], in the D-T reaction, the practical terms of reactor condition is:

$$n\ t\ T > 10^{21}\ (\text{keV}\ m^{-3}\ s)$$

Where t is the length of time, n is the ion density in the plasma, and T is the plasma temperature (between 10 to 20 keV).

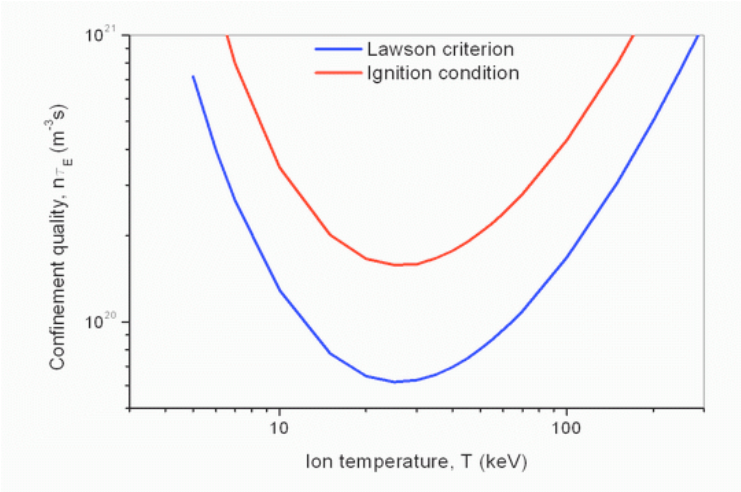

Fig. 1-3 Lawson criterion, the minimum value of confinement quality against temperature gives Lawson's criterion.

At such extreme temperature conditions, containing the dense plasma in an ongoing fusion reaction will be very challenging and most overcome the following:

1. Energy loss from unstable particles.
2. Unavoidable disturbances from plasma deviations
3. Equilibrium confinement forces to inhibit rapidly disassemble of the plasma

Also, in a Tokamak reactor, the controlled fusion reaction depends not only on continuous power production, but also on suitable first wall and structural materials. Thus, several candidate materials are attracting attention, including SiC.

1.2. Brief history of Silicon Carbide

Silicon Carbide (SiC), also known as carborundum, one compound of silicon and carbon. It was discovered by the Swedish chemist, Jöns Jacob Berzelius in 1824 [8]. This exceedingly hard, synthetically-produced crystalline compound with the chemical formula SiC, was firstly manufactured in a wide-scale in 1893 by Edward Goodrich Acheson. Meanwhile, natural SiC crystals were also found as a minor component in the Canyon Diablo meteorite in Arizona by Dr. Ferdinand Henri Moissan [9].

Since the early 20th century, SiC has been used as a material for grinding wheels, sandpapers, and cutting tools. With its high-temperature strength, low thermal expansion, and great resistance to chemical reaction, silicon carbide is very valuable for industrial applications. These include heating elements for furnaces, refractory linings, and wear-resistant parts for pumps and engines (turbine components), and even use as a semiconductor material. Considering its thermal properties and electrical conductivity, SiC was chosen as a semiconductor substrate for manufacture of light-emitting diodes. Since the last century, many commercial products (SiC based Schottly diode and high frequency metal–oxide–semiconductor field-effect transistors (MOSFETs)) have been launched into the market. [10; 11] Also, because of its great mechanical stability under high-energy neutron irradiation and high temperature conditions [12], SiC has great potential as either a structural material in advanced nuclear energy systems or tristructural-isotropic (TRISO) fuel particle coating material.

1.3. Physical properties of SiC

SiC has many excellent physical and chemical properties, besides the hardness and wear-resistance, typical silicon carbide characteristics includes:

- Low density and high strength
- Oxidation resistance
- Chemical resistance
- Good high temperature strength
- Low thermal expansion and high thermal conductivity
- Excellent thermal shock resistance
- Low neutron activation (i.e., minimal long-term radioactivity)

These excellent features of SiC make it widely used in nuclear engineering. The high thermal conductivity coupled with outstanding high strength give this material exceptional irradiation resistant quality. In applications for fission reactors, SiC can be used as a coating layer on nuclear fuel particles (e.g., TRISO fuel particles). This concept of nuclear fuel is used in high temperature gas cooled reactors (e.g., pebble bed reactor). Not only providing a structure support to the nuclear fuel, SiC is also the main diffusion barrier to the release of fission products.

At high temperatures beyond 1500 °C, SiC with minor or no grain boundary impurities can strongly maintain its strength. This resistance to chemical attack and strength retention at high temperatures has made this material an important candidate nuclear material in fusion applications. Primarily due to its inherently low activation under irradiation and radiation stability, SiC is considered for use as structural components for Tokamak reactors.

1.4. Crystal Structure of SiC

SiC is the only stable intermediate compound in the Si-C binary system, which has about 250 crystalline forms. As a covalent compound, the melting point of SiC is above 2500 °C (as shown in the phase diagram, Fig. 1-4) [13]. The C-Si bond has sp^3 hybridization with partial polarization, and the ionic character of the

C-Si bond is about 12 %. The electronegativity of silicon and carbon is 1.90 and 2.55, respectively.

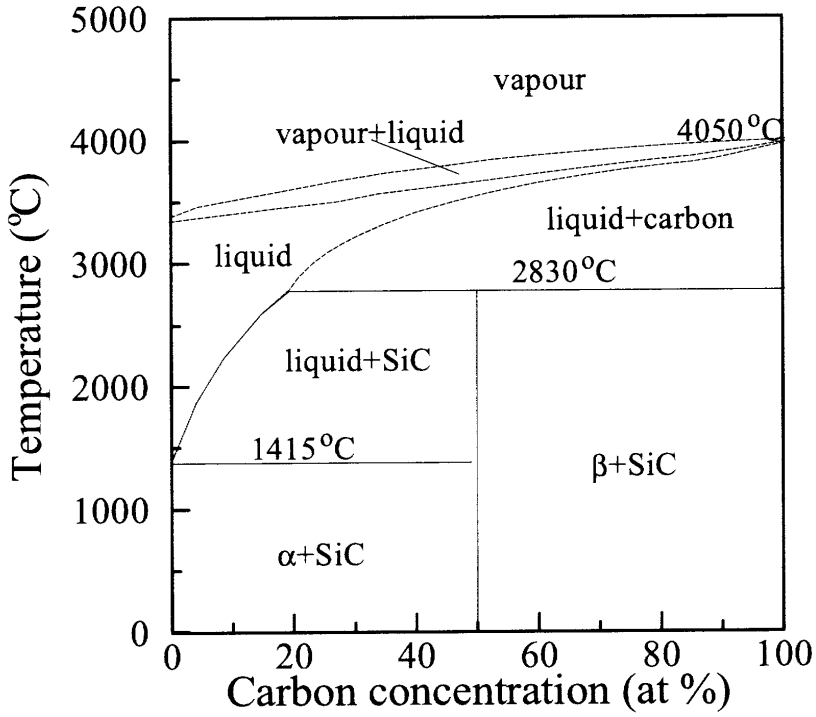

Fig. 1-4 Phase diagram of silicon carbide.

As is the case for many other compound materials, SiC exhibits a rich polymorphism, with a series of different structures. Generally speaking, the most common polytypes of SiC include: 3C, 2H, 4H, 6H, 8H, 9R, 10H, 15R, 19R, 21H, 21R and 24R. The number denotes the periodicity of close-packed stacking in the crystal. The symbol (C), (H) and (R) represent the three basic cubic, hexagonal and rhombohedral crystallographic systems, as summarized in table 1-1 and table 1-2. For example, 3C-SiC refers to the three-bilayer periodicity of the stacking (ABC) with the cubic symmetry (as symbol C indicates).

The most commonly observed polymorphs are alpha silicon carbide (6H-SiC) and beta silicon carbide (3C-SiC). The schematic diagram of the SiC unit cell is shown in Fig. 1-5 [1]. Basic parameters of SiC are summarized below. Both 4H

and 6H polytypes are widely used in the semiconductor industry, due their larger band gaps, and in research. Early mass-production of these 4H and 6H SiC is leading to advances in fast, high-temperature and/or high-voltage devices (Schottky diodes, MOSFETs…etc.).

Table 1-1 Crystal structure and lattice constant of different SiC poly-types.

Polytype	3C (β)	4H	6H (α)
Crystal structure	Cubic (Zinc blende)	Hexagonal	Hexagonal
Space group	T^2_d-F43m	C^4_{6v}-P6$_3$mc	C^4_{6v}-P6$_3$mc
Pearson symbol	cF8	hP8	hP12
Lattice constants (Å)	4.3596	3.0730; 10.053	3.0810; 15.12

Table 1-2 Stacking order, lattice parameters and densities of different SiC poly-types.

poly-types	Stacking order	Lattice parameters / Å			Density /g·cm^{-3}
		a	b	c	
3C	ABC…	4.359	4.359	4.359	3.215
2H	AB…	3.081	3.081	5.031	3.219
4H	ABAC…	3.081	3.081	10.061	3.215
6H	ABCACB…	3.081	3.081	15.092	3.215
15R	ABCBACABACBCACB…	3.073	3.073	37.700	-
21R	-	3.073	3.073	52.780	-

1.5. SiC composites and nano-engineered SiC

To enhance the mechanical properties, the SiC fiber reinforced SiC composite (SiC_f/SiC) was developed [12]. This composite is reinforced by advanced silicon carbide fibers with low oxygen content, high-crystallinity and a near-stoichiometric composition. With embedded woven fibers, its fracture toughness is greatly improved comparing to monolithic SiC. Therefore, SiC_f/SiC composites

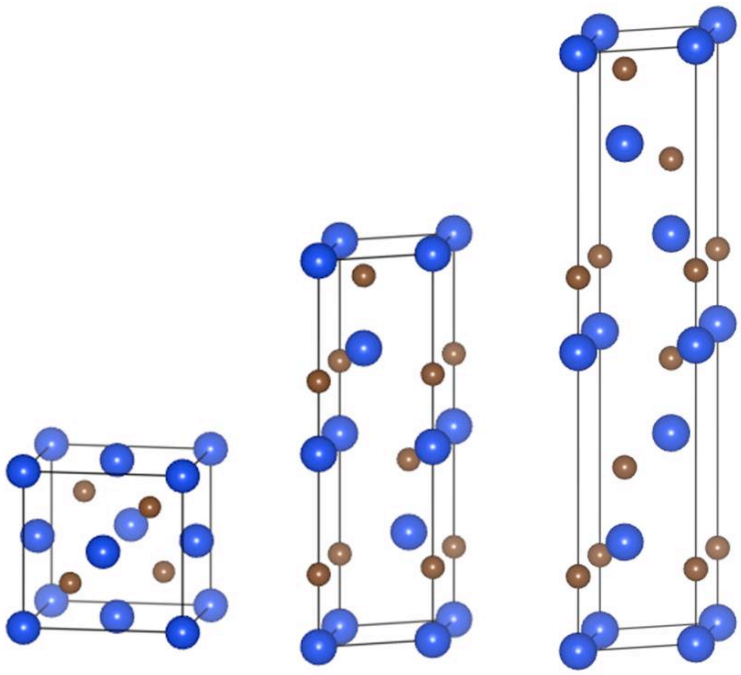

Fig. 1-5 Unit cell of 3C-, 4H- and 6H- SiC [1].

are being considered as structural materials for aerospace applications, high-temperature industrial applications, and nuclear reactor systems because of the lightweight, antioxidant stability, and most importantly for nuclear applications, minimal neutron activation combined with excellent mechanical properties at high temperatures. However, cracks in the interphase layer between fiber and matrix after irradiation have led to a number of unsolved issues.

Nano-engineered (NE) nanocrystalline SiC

Grain size reduction can improve the mechanical properties tremendously because of dislocation migration impedance at grain boundaries. Also, materials with larger grain sizes can contain more dislocations, which can accumulate and lead to a higher driving force for dislocations to move. Polycrystalline materials with micro-sized grains contain many grain boundaries, and grain size reduction is considered as a common way to enhance the yield strength of a material.

Unlike a polycrystalline structure with micro-sized grains, nano-engineered (NE) nanocrystalline ceramics, with grain sizes of about 100 nm, have attracted a lot of attention in research due to their superior physical properties. It has been reported that the nanocrystalline structure could tremendously change the optical, electrical and mechanical properties [14-19]. Recent investigations [20; 21] have shown that nano-engineered nanocrystalline (NE) SiC, which contains high-densities of stacking faults (SFs) parallel to the surface with nm spacing formed within a nano-sized grain structure (as shown in Fig. 1-6), can confine random point defect migration to the highly localized region between the SFs. In addition, recent simulation studies [22] of defect–GB interaction mechanisms have shown that GBs play a key role in capturing and emitting interstitials from the lattice. Therefore, the recombination of interstitials with the vacancies close to GB can be enhanced [23], and enhanced radiation tolerance can be expected in NE SiC due to the enhanced defect recombination and annihilation rate within the SFs layers.

Understanding grain boundary-dominated defect physics can lead to the discovery of new applications in a number of fields. In this dissertation, ion irradiation was applied to investigate the irradiation response of single crystal and NE SiC under conditions expected in a fusion reactor environment.

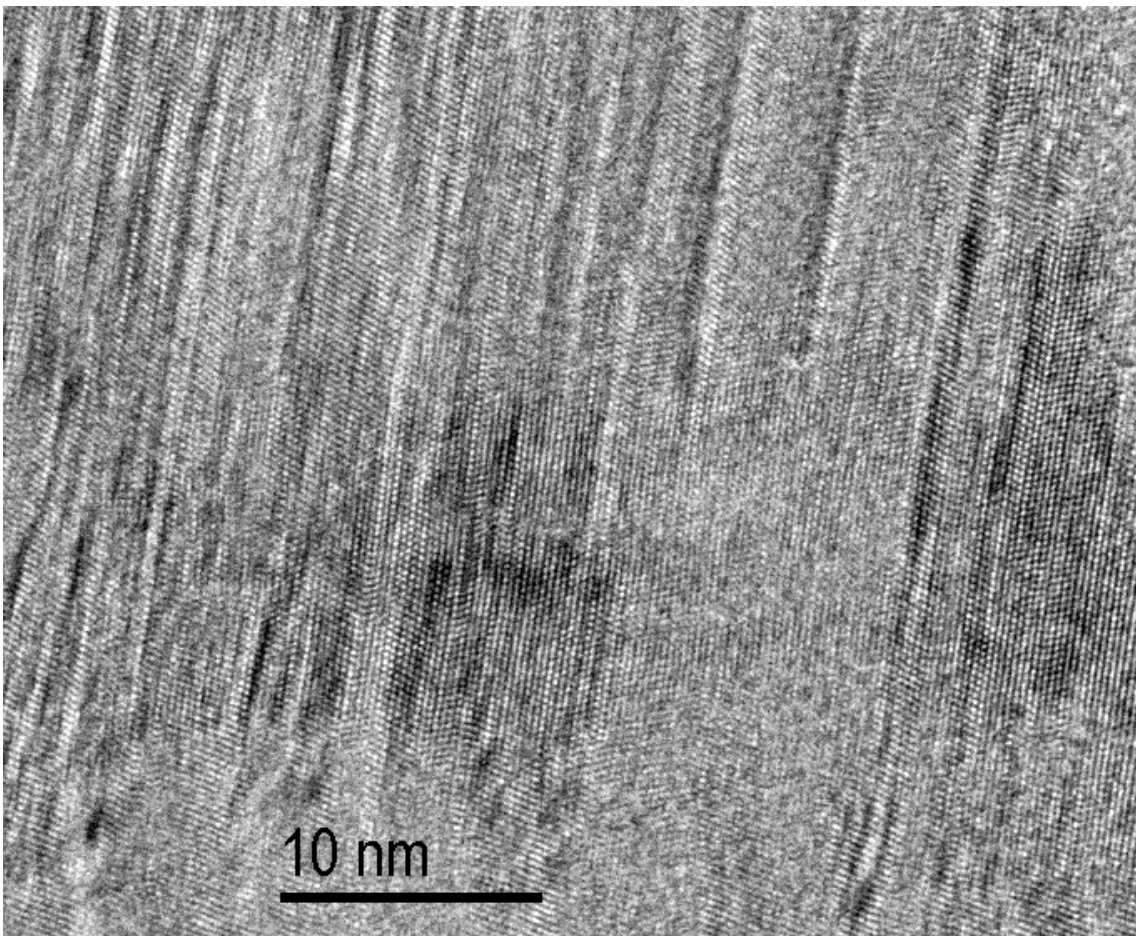

Fig. 1-6 Stacking fault layers within nano-sized grain structure in NE-SiC.

Chapter 2. Research Methodology

In this research, helium implantation and subsequent heavy-ion irradiation are performed to investigate the irradiation response of single crystal and nano-engineered (NE) SiC. Conventional and Time-of-Flight elastic recoil detection analysis (ERDA) are used to quantify the implanted helium concentration profile, since it is ideally suited for the analysis of helium in heavier targets. The helium depth distribution determined from the ERDA spectrum is compared with the predictions from the Stopping and Range of Ions in Matter (SRIM) code (version 2012) [24]. Cross-section transmission electron microscopy (TEM) analysis is used to determine the size and local density of bubbles and dislocation loops.

2.1. Ion-implantation and ion-irradiation

Stopping and Range of Ions in Matter (SRIM) simulation

The SRIM software package is widely used to simulate the interaction of energetic ion in matters. It provides useful predictions on implanted ion range distributions, as well as the depth profiles of energy loss (including partitioning between electronic and nuclear processes) and depth profiles of displaced atoms (or damage production), which are valuable for research on ion implantation, radiation damage in materials, and even in ion beam analysis. James F. Ziegler and Jochen P. Biersack first developed this program in 1983. Based on the Monte Carlo simulation methodologies, the binary collision approximation (i.e., the influence of neighboring atoms is neglected) is used, with a random number generator, to determine the impact parameter of the incident ion, and each recoil ion, for each successive collision. Therefore, the three-dimensional distribution of the incident ions in the solid, penetration depth, and atomic displacements along the ion trajectory can be simulated in detail. Other information, such as nuclear and electronic stopping power, energy deposition, sputtering rate, defect

concentration, ionization and phonon production can also be determined. The SRIM program is routinely modified and updated as of this date.

Ion-implantation

To tailor or modify the properties of materials, ion implantation with specific dopants, (i.e. ions or isotopes) is carried out to introduce property changes into materials. Ion-implantation is widely used in altering the chemical, magnetic, or electronic properties for industrial applications.

In this study, pre-helium implantation was performed in the Ion Beam Materials Laboratory (IBML) at Los Alamos National Laboratory, using a 200 kV ion implanter. Samples of the single crystal 3C SiC were implanted with 65 keV He^+ ions at 7° off the surface normal to avoid channeling conditions, and the NE SiC samples were implanted with 65 keV He^+ ions along the surface normal. Both types of SiC samples were implanted to three helium ion fluences (1×10^{15}, 3×10^{15} and 1×10^{16} cm^{-2}) at 277 °C, which is above the critical temperature for amorphization [25; 26], to avoid amorphization and retain the crystalline structure. The helium depth profiles and damage profiles for the Au ion irradiation are predicted using the SRIM code, and the peak in helium concentration is predicted to be at a depth of 330 nm from the surface.

Heavy-ion irradiation

Tandem Pelletron systems

To mimic defect evolution in a fusion reactor environment efficiently, the approach of ion-irradiation is chosen. Ion-irradiation can be used to conduct studies on the interaction of energetic ions with targets and subsequent effects on the properties and structure of the irradiated materials.

The selected ions are sputtered from specific cathodes after Cesium sputtering. Some of the sputtered materials gain electrons in passing through the cesium coating on the surface of the cathode, and form the negatively charged ion beam. With pre-acceleration energies of a few tens of keV, the negative ions are bent at a 30° angle by the injection magnet and then penetrate through an extractor, einzel lens and y-steerer before entering into the central beamline of the accelerator.

The accelerator used in this study is a 3.0 MV Pelletron (model 9SDH-2) tandem electrostatic accelerator, manufactured by National Electrostatics Corporation (http:// www.pelletron.com), located at IBML, University of Tennessee, Knoxville (Fig. 2-1) [27].

Fig. 2-1 3 MV tandem accelerator with two ion sources, three beamlines, and four end-stations in the Ion Beam Materials Laboratory (IBML) at the University of Tennessee (UT).

The negative ions coming from the ion source will be accelerated through the first half of the tandem accelerator before they reach the gas canal for electronic stripping. When negative ions interact with the stripping medium (nitrogen gas), the ions tend to lose electrons and are converted to positive ions. After the process of electron stripping, the now positive ions are further accelerated through the second half of the tandem accelerator. The positive charged ions with selected energy are then bent using the switching magnet into the

appropriate beam line (one of three beam lines) before entering the target chamber.

To compare and verify the critical dose for helium bubble formation under far-from-equilibrium irradiation conditions, subsequent irradiation with 9 MeV Au^{3+} ions was carried out in a multi-purpose target chamber in the UT-IBML facility. The dose in dpa is determined using SRIM2012, assuming a density of 3.21 g/cm^3. Although the threshold displacement energy is crystal-direction dependent, we assume displacement energies of 20 eV and 35 eV for the C and Si sublattices, respectively as a step function based on recommendations from a previous study [28]. In this study, irradiations to ion fluences from 7.8×10^{15} (10 dpa) to 2.3×10^{16} (30 dpa) cm^{-2} were performed, which produced a flat-damage profile of 10 to 30 dpa at the depth of interest, 250 to 500 nm from the surface, as shown in Fig. 2-2. A uniform rastered beam, with a constant particle flux of 2.3×10^{12} cm^{-2} s^{-1} (current density of 11.1 nA/mm^2), was used. A glass scintillator and a CCD camera, placed through a silica viewport on the multipurpose chamber, were used to accurately locate the ion beam on the sample.

The 9 MeV Au^{3+} irradiations have been performed at high temperature (700 °C) under high vacuum conditions (4×10^{-5} Pa). The temperature of the sample during irradiation, as well as during thermal annealing, is monitored and controlled using the HRN (LPS-800-1) heater controller from Thermionics Northwest Inc. [29]. The main thermocouple is located on the sample, and an additional one is connected to the sample holder, with the aim of accurately controlling the temperature during irradiation and thermal annealing processes.

During irradiation at 700 °C, a small part of each helium-implanted sample is masked to retain un-irradiated areas in order to investigate the separate effects of thermal annealing on helium migration and bubble evolution in the absence of irradiation. Such an approach ensures similar thermal conditions and provides a

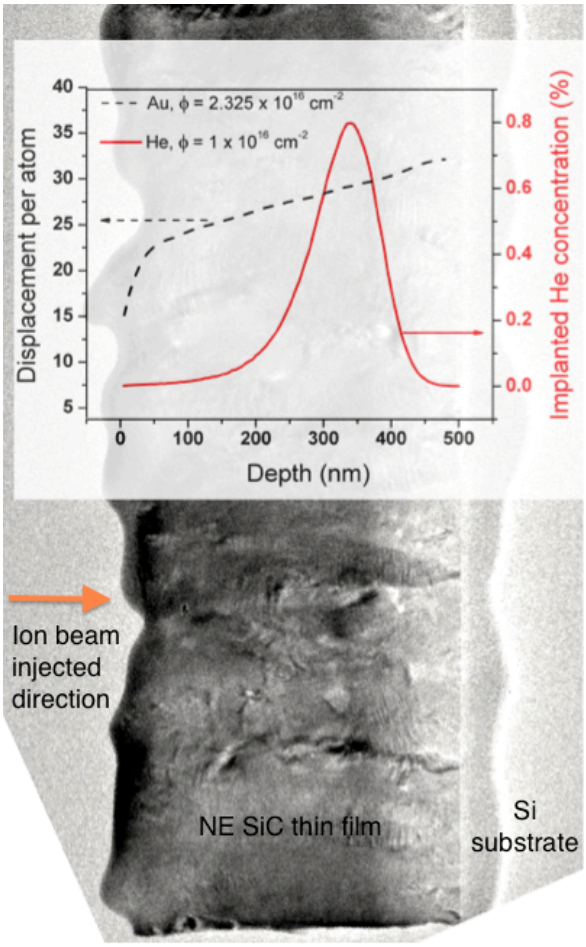

Fig. 2-2 SRIM 2012 simulation of the irradiation damage prediction and implanted helium concentration in NE SiC. The depth profile of SiC film on Si substrate is shown as a background TEM image.

more reliable comparison of helium evolution at high temperature with and without heavy ion irradiation.

2.2. Forward elastic recoil detection analysis

Elastic recoil detection analysis (ERDA)

The principle of conventional elastic recoil detection analysis is very similar to Rutherford backscattering spectrometry (RBS). Instead of detecting the projectile at the back angle, the detector is located in the forward direction to detect the recoils. Spectrometry of these forward recoiled atoms with different energies gives rise to the quantitative depth profiling of elements in the target. For acquiring the lighter element distribution in the target, a thin foil can also be placed in front of detector to block out heavier recoil atoms.

In this study, ERDA is used to quantify the implanted helium concentration profile, since it is ideally suited for the analysis of helium in heavier targets, such as SiC. Furthermore, ERDA has better mass resolution than RBS to detect light elements without background interference [30-32]. The helium depth distribution determined from the ERDA spectrum is compared with the prediction from the SRIM simulations (version 2012).

The experiment was performed at the UT-IBML in a high-vacuum chamber (1.3×10^{-5} Pa) to confirm the helium concentration profile in single crystal 3C SiC implanted at the highest helium fluence (1×10^{16} cm^{-2}). In this conventional ERDA measurement, an 11 MeV beam of O^{4+} ions impinges on the specimen at 75° off the surface normal, and a mylar foil with thickness 9.6×10^{19} atom/cm^2 (i.e., 10 μm) is placed in front of a Si detector to block the forward scattered or recoiled particles, except helium (see Fig. 2-3).

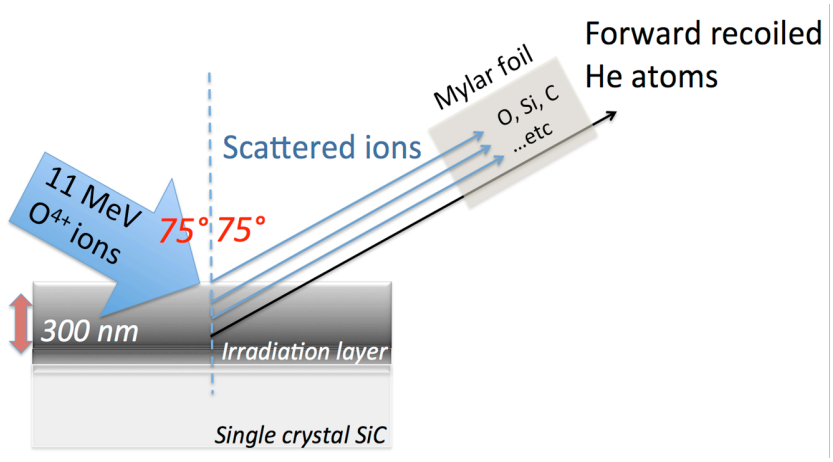

Fig. 2-3. Conventional ERDA experimental configuration with a mylar foil to block all heavy elements.

Time-of-flight (ToF) ERDA

For conventional ERDA, the energy detected from recoiled ions is dependent on the mass and depth of the target atom in the specimen. Thus, the interpretation of ERDA spectra can be complicated by mass-depth ambiguity. However, by measuring the recoil ion energy and mass independently, Time-of-flight elastic recoil detection analysis (ToF-ERDA) provides superior mass resolution for both heavy and light elements.

ToF-ERDA, complementary to RBS and conventional ERDA, can detect forward-scattered recoiling atoms from a single collision. Equipped with an energy detector and two ToF thin foil detectors at ToF1 and ToF2, as well as a well-defined corresponding ToF distance in a forward scattering geometry, the ToF ERDA setup can measure the velocity and energy of the recoiled atoms from the target simultaneously. The schematic diagram of the ToF-ERDA set up is shown in Fig. 2-4. Modification of foils can also be performed to make the system suitable for light element analysis. When the recoil atoms pass through the foil, secondary electrons are ejected and trigger a timing event within each ToF

detector.

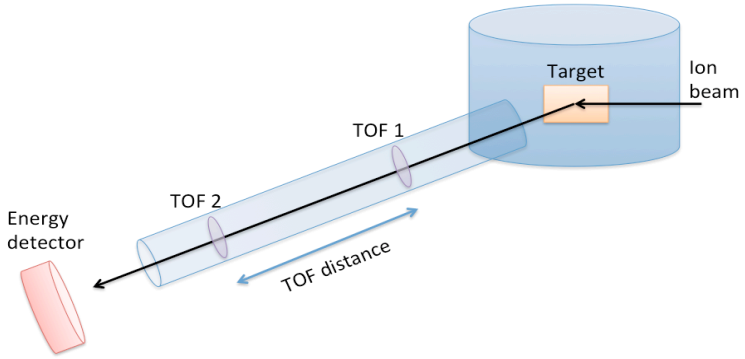

Fig. 2-4. Schematic diagram of Tof-ERDA set up.

With incident heavy ions (M_1>>M_2), the cross section for recoils is proportional to Z_2/M_2, approximately. Because the value Z_2/M_2 does not decrease dramatically as the atomic number decrease, the ToF-ERDA is able to distinguish signals from light recoils, including isotopes of hydrogen to carbon. Generally, incident ions for ToF-ERDA range from O to Au at tens of MeV.

2.3. Transmission Electron Microscope Sample preparation method

When conducting Transmission Electron Microscope (TEM) observations, the interaction between electrons of the beam and atoms of the samples lead to scattering events. To acquire sufficient intensity/number of transmitted electrons, a thin sample is required. The essential thickness depends on acceleration voltage, material properties, and investigation method. Samples for conventional TEM, STEM, and HRTEM characterization should be less than 100 nm. To perform quantitative EELS analysis, the thickness of the sample is generally between 0.3~0.7 times the mean free path of an electron in the sample, which is about 136 nm for 200 keV electrons in SiC [1]. For microstructural study, the appropriate preparation technique should have as little influence on structural

and chemical properties as possible. Two of the most common methods used for preparing cross sectional views of ceramic samples are introduced below.

2.3.1. Conventional Sandwich/Ion Milling Sample Preparation

1. A diamond saw is used to slice the sample into 2 mm wide strips that are attached face-to-face with M Bond 610 to create a sandwich structure (wafer/glue/wafer), keeping the surface/film of interest in the middle of the sandwich (as shown in Fig. 2-5).
2. Specimens are mounted onto a Pyrex stub using crystal bond; begin by polishing one side of the sample with MultiPrep Polishing System (as shown in Fig. 2-6).
3. Gradually switch the diamond lapping film from a coarse one to finer one. Lapping films with diamond particle sizes from 30, 15, 6, 3, 1, to 0.5 μm are used for rough to fine polishing of the specimen. A Multi-tex polishing cloth combined with 0.05 μm colloidal silica solution is then used for final polishing. Once the damage free surface is obtained, flip the sample over and start the second side polishing with the same progression of diamond lapping films, until the thickness of the sample is less than 10 μm.
4. The sample is then mounted on the TEM grid using M Bond 610. Wait until the epoxy is hardened.
5. To remove the sample from the polishing holder, the polishing holder is soaked in acetone until they are separated and no crystal bond remains on the sample.
6. Sample is ready for precision ion polishing (PIPS).

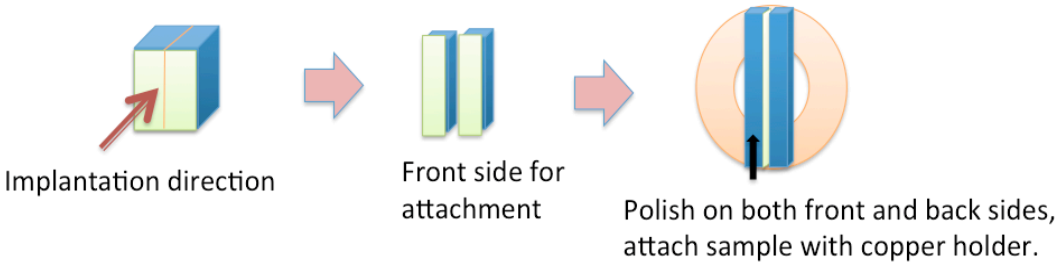

Fig. 2-5 The schematic of sandwich structure for thinning and polishing.

Fig. 2-6 The Multiprep system manufactured by Allied company. The sandwich foil can be polished down to 10 μm with this sophisticated equipment for the cross section sample polishing and thinning,

Precision ion polishing system (PIPS)

To get the sample thin enough for electrons to go through (<100 nm), the method most commonly used is mechanical polishing followed by ion milling.

Precision Ion Polishing System

The PIPS is carried out in this research using a Gatan 691 PIPS Ion Mill, as shown in Fig. 2-7. A step-by-step procedure is provided below:

1. Load the sample in PIPS holder, the region of interest should be centered in holder. Then load the PIPS holder into the airlock chamber.
2. To initiate the flow of Ar gas into PIPS, open the valve of the pressurized Ar gas cylinder.
3. Pump down the airlock chamber, lower the receiver into the PIPS when vacuum is ready
4. Use the following conditions as typical when perform ion milling
    1. Ion gun tilt angles: ± 3 ° or ± 4 °
    2. Rotation speed: 1 to 3
    3. Accelerating voltage: 2 to 4 kV
5. Turn gas controllers (on the front PIPS panel) on to start ion milling.
6. Unload the sample when the specimen polishing is complete.

Fig. 2-7 Gatan 691 PIPS ion mill machine.

2.3.2. Focused Ion Beam Milling Sample Preparation

Due to the high efficiency and small sample consumption, focused ion beam (FIB) methods are widely utilized today for TEM sample preparation.

With a Ga liquid metal ion source (LMIS) operating at accelerating voltages ranging from 30 to 1 keV, the FIB can precision sputter atoms from the target material to either cut or polish a cross section at any point of interest desired on the sample. Most commercial instruments have combined the ion column with an electron column to monitor the thickness during sample preparation. Procedures are summarized below:

1. Vent the chamber for sample loading. After loading the sample, wait for a vacuum of better than $2x10^{-5}$ Torr before opening the column valves.
2. Move to an appropriate working distance and align the coherent point and eucentric height. It can prevent the image from moving laterally as the specimen is tilted.
3. Calibrate the relative positions of the e-beam and ion-beam images.
4. For sample cutting with the ion beam, deposit a Pt layer to protect the surface of the sample, and set all the parameters for cutting two trenches to make a thin lamella; choose an appropriate current for cutting.
5. Lift out the lamella and mount it on the TEM lift out grid.
6. Perform the final fine polishing (5 or 10 kV) with low ion current, until a transparent area can be found under 3 keV SEM observation.

2.4. Samples

The materials used for this research are single crystal 3C SiC thin film, with a thickness of 1000 nm on a Si substrate (CVD process by NOVA SiC, France), and NE SiC films that contain a high density of <111>-type stacking faults (spacing of 1 to 2 nm) within columnar grains of 100 to 300 nm size grown along

the <111> direction. The NE SiC films were grown on Si (100) wafers by low-pressure chemical vapor deposition with an average film thickness of 532 nm. Details of the processing technique for the NE SiC are provided elsewhere [20]. The cross-sectional TEM samples are prepared by mechanical polishing. Additional ion milling (5 to 3 keV Ar^+ ions at an angle of 85° off the surface normal) is performed as necessary to achieve an electron transparent region in the specimens.

2.5. Transmission Electron Microscopy

The macroscopic effects of irradiation are the results of interactions occurring at the atomic scale; thus, it is necessary to understand how the microstructures of irradiated materials evolve. A numbers of strategies, for example X-ray diffraction, Neutron diffraction, Raman spectroscopy, Ion-beam analysis or Nano-indentation, have been employed among other techniques to investigate fundamental damage mechanisms. Depending on the irradiation conditions, irradiation-induced defect clusters may include interstitial and vacancy dislocation loops, precipitates, voids or bubbles, all in a size range on the order of nanometers. Since irradiation may induce both compositional and structural changes, a direct observation technique at the nanometer scale is needed.

Because the Transmission Electron Microscope (TEM) is capable of imaging at magnifications on the order of 10^5 with resolution better than 1 nm, small defect clusters can be imaged and analyzed. Some TEMs are combined with *in-situ* ion irradiation capabilities, providing real time direct observation during irradiation.

In this study, a Zeiss Libra 200 HT FE MC TEM at an acceleration voltage of 200 kV with a Zeiss Omega energy filter was employed to analyze the microstructure of the SiC samples. The illumination system of this TEM incorporates a three-lens condenser system for homogeneous and parallel TEM wide-field illumination

independent of illumination intensity. The electron beam emitting from the source—the high efficiency Schottky field emission gun—is filtered with an in-column monochromator (MC) and Omega energy filter. With this monochromator, the energy resolution (determined by measuring the full width at half maximum of the zero-loss peak in vacuum) of the EELS spectrum acquired by Libra 200 MC is better than 0.3 eV, as shown in Fig. 2-8 [1]. In this study, to carefully quantify the helium K-edge signal, energy resolution from 0.17 to 0.2 eV with an energy dispersion of 0.025 eV is applied. The information from inelastic scattering electrons can be analyzed from the integration of the imaging energy spectrometer. The 2nd order corrected and 3rd order optimized aberrations spectrum can be acquired for improving the quality of imaging and diffraction signals [33].

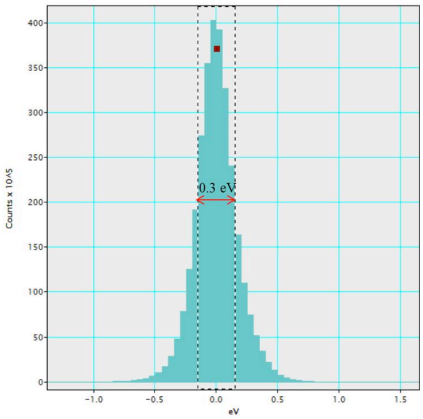

Fig. 2-8 Energy resolution from zero loss peak of EELS spectrum taken with Libra 200 MC TEM, energy resolution is better than 0.3 eV [1].

Bubble quantification

To acquire high quality TEM images, microscope alignment and image correction need to be performed meticulously. A standard TEM alignment procedure includes illumination centering, aperture centering, focusing, and astigmatism correction. After careful TEM alignment, small defects like helium bubbles can be

identified using through-focus imaging on the cross-sectional samples, as illustrated in Fig. 2-9.

It was reported by Jenkins *et al.* [34] that because of the structure factor contrast under dynamical or bright-field kinematical imaging conditions, bubbles with diameters larger than 5 nm can be imaged at in-focus condition. In contrast, out-of-focus imaging is probably the only way to image smaller size bubbles. Because of the phase shift between electrons traveling through bubble and electrons traveling through matrix, the Fresnel fringes will appear at the edge of bubble. Under kinematical conditions, bubbles appear as dark/bright dots surrounded by a bright/dark Fresnel fringes at an over-/under- focus condition. However, the through focal images of bubbles are strongly influenced by the defocus value.

It was reported by Rühle and Wilkens (1975) [35] that by measuring the inside edge of the first dark Fresnel fringe, the bubble can be delineated reasonably well for either sphere or faceted voids. In addition, it was also reported by Rühle and Wilkens [35] that with a under focus value from 800 to 1000 nm, by measuring the first Fresnel fringe, the measured size will correspond to within 10 % of the actual size. Therefore, in this work, all images for void/bubble analysis were recorded in a slightly underfocused condition (with a defocus value of about 900 nm, far away from the Scherzer defocus condition). With the bubble sizes measured based on the first dark Fresnel fringe, data from this work can be compared with other literature results.

The rough background of NE SiC sample is not sufficiently smooth for automated defect counting and sizing; thus, manual defect counting and sizing is applied in this work. Although most of the bubbles observed in this work are spherical, by calculating the square root of the product of the longest inner diameter, d_1, and

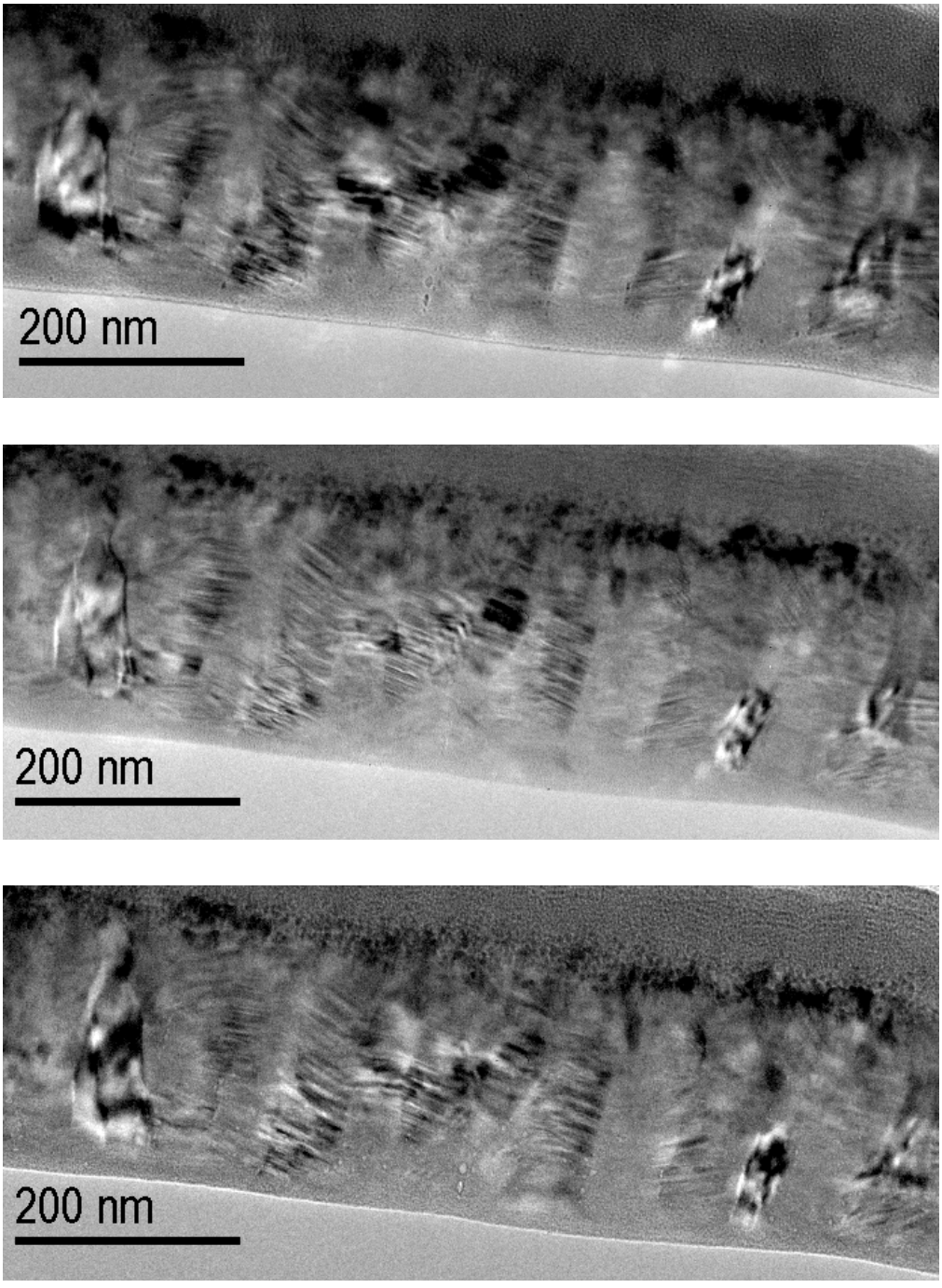

Fig. 2-9. Through-focus cross-sectional TEM images of NE SiC after helium implantation and post-Au irradiation to 10 dpa at 700 °C. (top) Over-focused with defocus value of about 900 nm, (middle) in focus, and (bottom) under-focused with defocus value of about 900 nm.

the shortest inner diameter, d_2, an average diameter of each bubble, $(d_1 d_2)^{0.5}$, can be estimated. Since some bubbles are not perfectly round, several TEM images were taken to obtain an average diameter at each condition.

2.6. Atomic Resolution Electron Energy Loss Spectroscopy (EELS)

When an electron beam interacts with a TEM specimen, both elastic scattering (Coulomb interaction with an atomic nucleus) and inelastic scattering (Coulomb repulsion by inner- or outer-shell atomic electrons that are excited to a higher energy state) occur. After passing through the magnetic prism, these scattered electrons are separated by their kinetic energies to produce Electron Energy Loss Spectroscopy (EELS).
In a typical energy-loss spectrum, there are three main sections:

1. Zero Loss Peak (Elastic scattering).

2. Low-Loss Region (Inelastic scattering of outer shell electrons, can be used to conduct a thickness measurement).

3. High-Loss Region (inner-shell ionization process via inelastic scattering, which provides characteristic ionization edges).

Since inelastic interactions include phonon excitations, plasmon excitations and inner shell ionization, and the energy needed to remove an inner-shell electron from an atom is known, the elemental components of a material can be determined. Combining the above information with the scattering angle, types of atoms, the numbers of atoms of each type and the dispersion relation of the material, the excitation caused in the inelastic scattering can be acquired.

Fig. 2-10 is a schematic diagram of STEM operation with simultaneous EELS acquisition. As the electron beam probe scans across the sample, the high angle

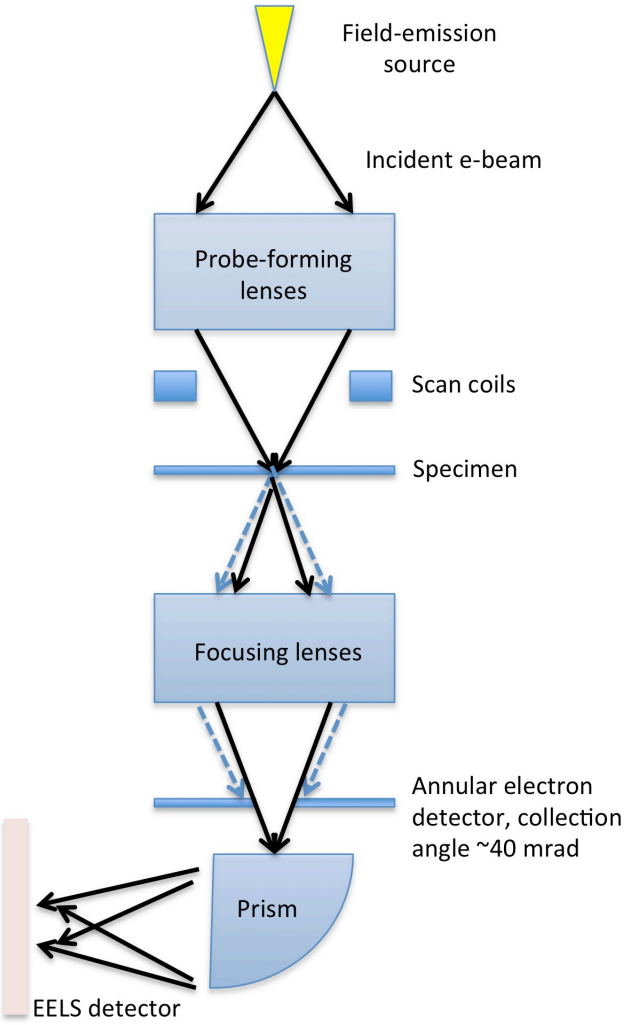

Fig. 2-10 A schematic diagram for TEM-based energy-loss spectroscopy: scanning-transmission (STEM) system. After electron interacting with the sample, a HAADF detector detects high angles scattered electrons and other electrons are collected to form an EELS spectrum.

scattered electrons are detected by a high-angle annular dark-field (HAADF) detector, and the other electrons passing through the central hole of a HAADF detector are collected and passed through the magnetic prism to form the EELS spectrum. The plasma information and sample thickness can be extracted from the low-loss structure of EELS spectrum. On the other hand, the concentration of a certain element in the sample and the bonding state can be extracted from the core-loss spectrum.

EELS spectra quantification

In STEM mode, spectra can be acquired from the center of the helium bubble and from the nearby matrix. In this study, to improve the signal-to-noise ratio, several of spectra are acquired for each bubble and averaged.

To deconvolute the experimental spectra, the Quantifit program [36] has been carried to perform the standard quantification. Using this program, the zero-loss, low-loss and core-loss spectrum can be fitted by the ionization edges and background, more details are provided elsewhere [36; 37]. The helium K-edge position can then be determined from low loss plasmon peak.

It is worth noting that for fitting the zero-loss peak, a product of two Lorentzian peaks was employed. Those two peaks are carried to show intrinsic energy distribution and asymmetric tail of zero-loss peak, respectively. On-the-other-hand, according Egerton *et al*. [38], the plasmon loss can be approximated by a Lorentzian function. Thus, the plasmon loss can be fitted using a Lorentzian function to extract the helium K-edge from it.

It is worth noting that to compare with previous study by Frechard *et al.* [39], the helium K-edge peak shift is determined by the peak position of the Gaussian fit after subtracting the background. Taking into consideration that the energy shift

was determined using the onset position of K-edge (using second derivative calculation to find the inflection point) in Walsh's work [40], a minor error may occur in estimating the amount of energy shift.

2.7. Intermediate Voltage Electron Microscope (IVEM)-Tandem Facility

To better understand the evolution of helium bubbles and *in-situ* defect formation [41; 42] under irradiation at higher temperatures, the IVEM-Tandem facility equipped with a Tandem accelerator (manufactured by National Electrostatics Corp) and high resolution Hitachi 9000 NAR TEM system is used. The Tandem accelerator provides several ion beams from protons to Au with a beam energy from tens keV (single-charged ion) to 1 MeV (double-charged ion). An uniform ion beam can be obtained on irradiated specimen using raster scanning. In addition, Ion dosimetry can be precisely measured with a Faraday cups below the stage. Details are provided elsewhere [41].

The TEM sample is loaded on a double-tilt high temperature (20 to 900 °C) Gatan sample holder. During irradiation, the microscope is operated at 300 kV with a point resolution of 0.25 nm. Microstructural observation is recorded with a Gatan 622 video rate camera and a Gatan Orius SC 1000 CCD camera with Digital Micrograph software.

The advantages of using IVEM-Tandem system are

- Real Time observation of structural evolution during irradiation or thermal treatment.
- Producing high-dose ion irradiation in several hours.
- Variable experimental conditions (temperature, ion type, ion energy, flux, dose, and applied strain).

The samples can be irradiated at incremental ion fluence to the desired range (i.e., in the pre-helium implanted region) to characterize the real time evolution of bubble size and density at each temperature and dose. These results can be compared with ex situ irradiation experiments, which will be helpful in identifying the peak swelling temperature in the samples under these irradiation conditions.

Chapter 3. Literature review of helium bubble in SiC

Advanced materials can enable reactor performance improvement, in particular by enhancing thermal creep resistance, high temperature strength and superior radiation damage resistance. Major fusion facilities, including the National Ignition Facility and ITER [43; 44], are focusing on exploring the remaining plasma physics issues near reactor-relevant operating conditions. Although SiC has great potential combining with great safety and waste disposal margins, as well as outstanding thermodynamic efficiency, it is still not fully developed for large-scale structural applications.

According to the current design of fusion reactor, SiC can be used as a structural component of the advanced blanket system or as a structural component. Substantial numbers of atoms of structural material are displaced from their lattice sites over the projected operating lifetime by energetic neutrons from nuclear reactions. The evolution of radiation damage from these ballistic collisions can be understood in terms of the displaced atoms that result in atomic defects, such as vacancies (vacant lattice sites) and self-interstitial atoms. In addition, gas atoms (helium and hydrogen) generated by (n,α) and (n,p) nuclear reactions can significantly impact the evolution of radiation damage. Due to the migration, interaction and aggregation of interstitials, gas atoms and vacancies, defect clusters, such as dislocation loops, gas bubbles and voids can form, leading to swelling and local deformation. These irradiation induced defects, defect clusters and deformation-produced network dislocations can lead to post-yield strain hardening effects. Combining with thermal annealing effects, dislocation gliding or point defect annihilation can also take place to eliminate defects at temperatures above 0.3 T_m. However, with different types of crystal structures and irradiation conditions, various types of irradiation-induced defects can form and resist thermal annealing to high temperatures.

As reviewed in the literature [12; 45-48], the damage rates of several neutron irradiation facilities (current and proposed) are summarized in table 3-1. The helium and hydrogen production in a reactor is dependent on the neutron energy spectrum; thus, the gas production in a tokamak system is a function of depth through the blanket, as shown in Fig. 3-1 [12]. The helium production is approximately 2000 appm/ MW-a/m^2 at the surface of the first wall and gradually decreases at deeper regions. For fission neutron irradiation studies of SiC, the gas atom production rates are reported to be 2.5 appm He/dpa and 3.3 appm H/dpa, respectively [49]. However, the production rate in a fusion reactor is much higher. It was reported that the first wall is predicted to be exposed to gas atom production rates of 130 appm He/dpa and 50 appm H/dpa [12]. Although the radiation resistance of SiC composite materials has been demonstrated under high temperature (300 to 800 °C) irradiation with fission neutrons up to 40 dpa [50], the production of gas atoms, which is not accounted for, can be expected to play a critical role in the evolution of voids or gas bubbles, leading to significant swelling and degradation of grain boundaries and interfaces.

3.1. Damage accumulation due to irradiation

Ion-atom or atom-atom scattering collisions are governed by interactions between atomic nuclei that are screened by the electron cloud surrounding them. These interactions can be described by interatomic potentials. In the case of the hard sphere approximation (i.e., $V(r)=0$ when $r>r_0$ and $V(r)=\infty$ when $r<r_0$) there is no potential function, which is unrealistic for ion-ion scattering, but is a very good description for neutron scattering collisions with atomic nuclei. For ion-ion interactions, different potential functions have been developed for collision kinematics calculation, and are based largely on screened Coulomb interactions. In the simplest case of elastic scattering, the recoil energy T from ion/neutron-nucleus interaction is given by

Table 3-1. Summary of damage rate per full power year (fpy) and irradiation parameters for neutron irradiation facilities.

	ITER	DEMO	IFMIF
Fusion power (GW)	0.5~1	2~4	3~4
First wall neutron loading (MW/m^2)	0.5~1	2~3	2~3
Integrated First wall load (dpa)	2~10	3~8	10~15
Helium production (app/FPY)	114	198	250~600

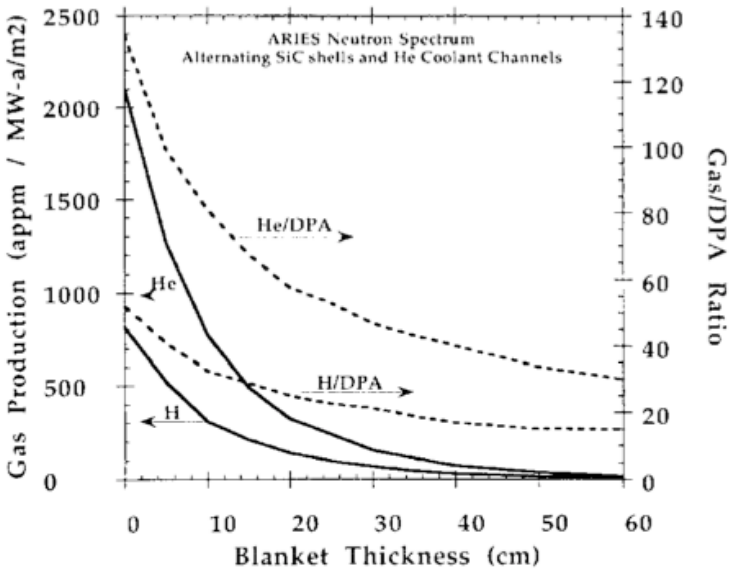

Fig. 3-1 Gas atom production dependence of neutron energy in a SiC blanket.

$$T = \frac{\gamma}{2} E(1 - \cos\theta)$$

Where we define $\gamma = 4mM/(m+M)^2$

When $\cos\theta = -1$, the maximum recoil energy can be obtained as

$$T_m = 4mME/(m+M)^2$$

The energy transfer to both atomic nuclei and electrons in the solid can result in displacements of atoms and local ionization. At high ion energies (E ~ 1 MeV/amu), electron energy loss dominates, with intense ionization, which can cause damage production or damage recovery [51-53]. For low ion energies (E < 0.1 MeV/amu), the nuclear energy loss dominates and leads to a local cascade of atomic collisions. In this study, the evolution of microstructure in SiC under fusion reactor environments is investigated, and the interaction of energetic ions and neutrons with solids is mainly focusing on energy transfer processes on the atomic structure from ballistic collision cascades. Therefore, the values of electronic energy loss in ion irradiation experiments are considered negligible in this study.

In a recent study [54], it was concluded that the radiation-induced amorphization of SiC due to electron radiation can be attributed to the accumulation of displacement damage rather than ionization effects. The maximum recoil energy T_m is given by

$$T_m = 2E(E + 2m_0c^2)/Mc^2$$

Where E and m_0 are the energy and rest mass of the electron particle. M is the mass of the displaced atom and c is the velocity of light.

3.2. Irradiation effects with thermal annealing

In the absence of suitable fission or fusion neutron test facilities capable of achieving the high neutron fluences expected in advanced reactors, ion implantation and irradiation techniques can be used to investigate the effects of high helium content and high irradiation doses in SiC. It has been reported from MD simulations that point defects and dislocations can be formed during irradiation at room temperature. The number of C defects (vacancies and interstitials) is 2–3 times as large as the number of Si defects, after the damage cascade has quenched. Antisite defects (i.e., with C site occupied by Si or Si site occupied by C) were also found, which play a significant role in driving radiation-induced amorphization of SiC [55]. With lower ion fluences and damage dose (about 0.1 dpa), defect recovery and annihilation and a defect-stimulated recrystallization process were observed [56]. The critical temperature for amorphization is estimated to be 227±10 °C for 6H-SiC under 2 MeV Au^{2+} irradiation conditions [25]. Above this temperature, SiC cannot be driven fully amorphous under irradiation. However, formation of radiation-induced voids is expected only at much higher temperatures (above 1000 °C), since one type of vacancy become sufficiently mobile in SiC above this temperature [57]. Amorphous SiC starts to recrystallize under irradiation at temperatures above 900 °C, and this critical temperature of recrystallization changes as a function of the energy transferred to recoils per atom and unit length [58]. Right before the recrystallization point, volume reduction and densification can be observed, which correlates with the reduction of antisites [59].

Planer channeling effects in varies types of SiC has been studied previously [60]; to avoid the channeling effect, single crystal specimens must be tilted at minimum angles off the zone axis. The flux dependence on amorphization dose was also discussed previously [54]. Since ionization effects may induce local thermal annealing effects, it has been suggested that for systematic studies, all

irradiations should be performed at a constant ion flux to avoid a flux dependence.

3.3. Helium in SiC

Previous experiments have focused on several aspects of helium irradiation effects and implanted helium behavior in 3C [61-65], 4H [66-72], 6H [63; 73-81] single crystal, poly crystalline SiC [82-84] and SiC_f/SiC composite [48; 85-94] for high-radiation environment applications, such as next-generation nuclear energy systems. These studies include

(1) Helium implantation in SiC at room temperature.
(2) Room temperature implantation followed by thermal annealing.
(3) High temperature helium implantation.
(4) Dual or triple ion beam irradiation.

Using different approaches, damage induced by helium implantation was investigated along the ion path (mostly conventional transmission electron microscopy).

3.4. Room temperature helium implantation

Studies of helium ion implantation in SiC with fluences from 10^{13} to 10^{17} ions cm^{-2} at room temperature have been reported over the past decade. In a implantation induced amorphous layer (high energy helium ion with about 1 dpa damage level), local strain and helium bubble formation in SiC were observed [68]. Compared with the threshold helium bubble formation concentration in Si (1.2 at. %) [95], the threshold concentration in SiC under irradiation is much higher. For single crystal (3C, 4H), the threshold helium concentrations for bubble formation at room temperature are 1.7 [61] and 2.7 at. % [66], respectively. For polycrystalline SiC, due to more nucleation sites provided by grain boundaries,

the threshold for bubble formation is higher than 8 at. % [64]. At room temperature, the critical dose for bubble formation exceeds the dose for amorphization, therefore bubbles could be observed in amorphous layers [70]. For 3C single crystals, subsurface blistering occurred for specimens irradiated to helium fluences greater than about 15 at. %. As fluences exceeding 40 at. % implanted gas, surface exfoliation was observed [61]. Helium atoms were preferentially incorporated in tetrahedral interstitial sites T_{Si} and T_C [73].

3.5. Thermal annealing and high temperature implantation

Helium implantation at elevated temperature and post implantation annealing have been performed to study thermal activated bubble formation. The threshold concentration for bubble formation is reduced tremendously, as shown in Fig. 3-2. P. Jung [63] has reported that after thermal annealing above 1250 °C for one hour, bubbles with observable diameter (larger than 1 nm) can be found in pre-helium implanted 3C and 6H single crystal SiC with a helium concentration of 0.06 at. %. Helium is trapped in the grain interior as two-dimensional disks of bubbles in the close packed direction, i.e. in habit planes (0 0 0 1) in 4H-SiC and (1 1 1) in 3C-SiC. This can be explained as a temperature dependent helium migration mechanism. Below the temperature of vacancy mobility, helium accumulation is occurs interstitially or as highly-pressurized helium-vacancy clusters, which may grow in a non-isotropic manner in some low-index planes and form planar bubbles. As the bubble size exceeds a critical value, the helium platelets can be transformed into planar clusters of bubbles [67].

At 1000 °C, helium implantation leads to the formation of platelets, which transform into planar clusters of helium bubbles after thermal annealing above 1227 °C [63; 76]. This suggests that the local helium/stable trap sites can effectively affect the formation and evolution of bubbles. It was also reported that

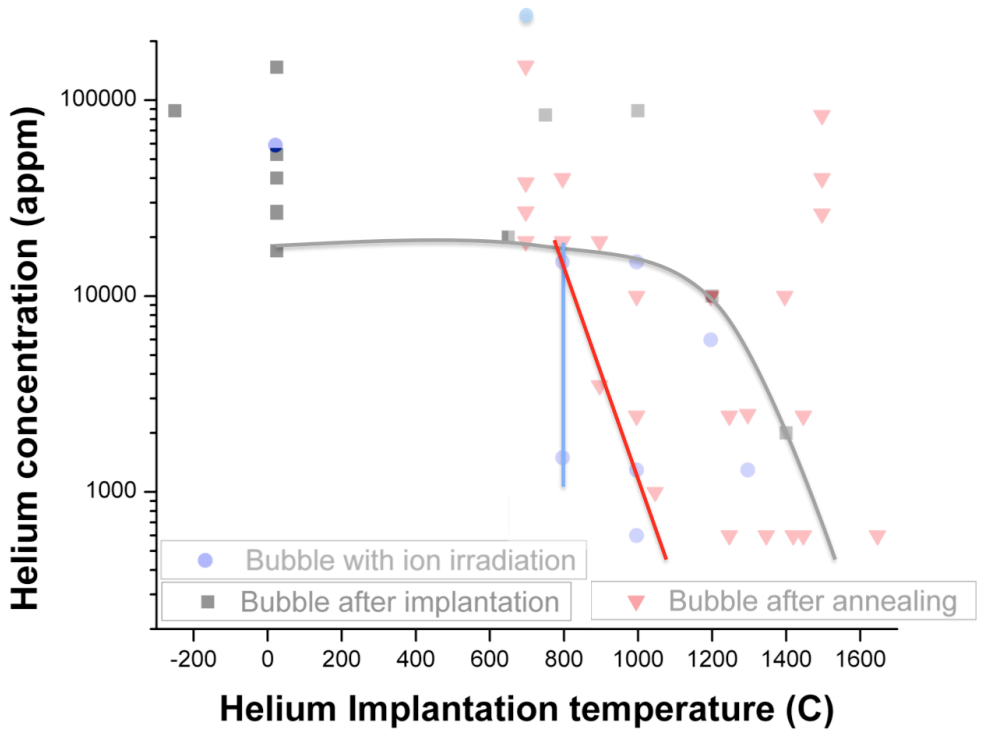

Fig. 3-2 Critical helium concentration for bubble formation in SiC under different irradiation conditions from the literature.

growth of helium bubble could be inhibited by displacement damage under irradiation in 4H and 6H SiC. Due to the production of Frenkel defects from irradiation and ballistic collisions of recoils with helium atoms in bubbles, helium atoms can be knocked out of the bubbles by the collision cascades, which allows the bubbles to re-equilibrate by loss of vacancies and results in a net reduction in mean bubble diameter.

As the temperature exceeds 1700 °C, a helium release peak appears and increases rapidly, suggesting significant helium migration behavior under high temperature conditions [87].

3.6. Dual and triple ion beam irradiation

To emulate the harsh fusion reactor environment, accelerator irradiation experiments including single, dual, and triple-beam ion beam irradiation have been conducted to investigate sequential and simultaneous helium implantation and ion beam damage accumulation. Most of the studies employed high-energy self-ion (i.e. silicon) to induce damage in SiC. Considering the production of hydrogen by (n,p) reactions in a reactor, hydrogen ion implantation is also employed to study the effects of gas atoms on microstructural evolution. The concentration/damage ratio was determined with the gas production rate in the reactor, which was previously mentioned (He/dpa and H/dpa respectively equal to 130 and 50 appm/dpa) [12]. Damage dose rates from 10 to 100 dpa have been carried out in these studies.

It has been reported that hydrogen atoms in the SiC_f/SiC composite will enhance cavity nucleation [89]. The average size of helium bubbles decreases with increasing concentration of hydrogen. The number density of helium bubbles increases with increasing irradiation temperature and implanted hydrogen concentration. Also, at irradiation temperature of 1000 °C, helium bubbles were

not observed in the matrix irradiated by single Si ions or single helium ions while helium bubbles were observed in the matrix irradiated by dual or triple ion-beams [48]. Thus, a hydrogen enhanced bubble nucleation and bubble growth suppression has been validated.

3.7. Helium Diffusion

E. Oliviero [62] has reported that at temperatures above 323 °C, interstitial helium and clusters of interstitial helium become mobile and can be trapped in pre-existing shallow structural defects. When temperatures are above 923 °C, the de-trapping of helium from helium-vacancy clusters can gradually occur. It has also been reported by T. Sauvage [75] that helium diffusion and broadening effects were found in 6H SiC using Nuclear Reaction Analysis technique after sample annealing at 1300 °C. NRA measurements also revealed a total helium release from single crystals, while 95 % is retained in polycrystals implanted and annealed under the same conditions (1300 °C/ 1 hr) [74]. H. W. Scholz has claimed that the vacancy mobility is extremely low below 1200 °C in SiC_f/SiC [85]. All of the previous studies have indicated that low helium migration would limit helium bubble formation at low temperatures. Therefore, thermal activated helium diffusion will play an important role in the bubble formation mechanism.

3.8. Grain size effects

The crystallized SiC fibers have smaller grains and much more grain boundaries than the SiC matrix. It was reported by T. Taguchi [96] that under triple ion beam irradiation, helium bubbles and cracks were not observed in Hi-Nicalon type S (HNS) fibers and Tyranno SA (TSA) fibers. On the contrary, helium bubble formation occurs only in the SiC matrix. The average size of helium bubbles is almost the same in SiC matrices of both composites. It has also been shown that

in low dose dual beam irradiation experiments, bubble formation occurred in the matrix only [89]. It can be concluded that the smaller grain size of the HNS fibers offers more potential nucleation sites for cavities due to the high grain boundary density. Hence, bubble growth behavior in the fiber is not as significant as in the matrix. Therefore, the number density of helium bubbles in the fiber exceeds that in the matrix [46].

3.9. Grain boundary behavior

The influence of grain boundaries on helium retention in **α**-SiC polycrystalline has been demonstrated [74]. Compared with helium implantation in single crystals, polycrystalline SiC displays the formation of intragranular over-pressurized bubbles. DFT calculations of helium bubble pressure has been performed, suggesting that the pressure of nano-sized bubble is about 0.8 to 1 GPa [97]. With the helium bubble formation at grain boundaries, this may lead to fracture and irradiation-assisted stress corrosion cracking (ICACC). In bending tests of SiC_f/SiC composites after high temperature implantation (950 °C) up to a helium concentration of 2500 appm, it has been shown that the strength of the material decreases by 38 % [98].

3.10.Swelling

The swelling behavior of helium implantation and ion-irradiation in previous studies indicated that the main factors of volume swelling can be attribute to both the number of anti-sites and the helium concentration. From stainless steel irradiation experiments using neutron and helium ions, tensile test showed significant mechanical property reduction [99].

For neutron irradiation, it has been reported by L. L. Snead that the volume

swelling at 1000 °C at a neutron fluence of 10^{29} cm^{-2} is about 0.5 at. % [86]. Compared with neutron irradiation, swelling induced by high fluence helium implantation in SiC at different temperatures has shown a similar swelling behavior. In a room temperature helium implantation experiment, the density reduction is about 15 % as amorphization occurs at a fluence of $1-2\times10^{16}$ cm^{-2} [100]. At 600 °C, amorphization does not occur. It was suggested that additional point defects created during the implantation have been annihilated. In addition, strain saturation was observed in the near-surface region. In the high-energy deposition region, the value of strain is no larger than 6 % [100].

It has been reported by Y. Katoh [101] that fusion-relevant helium production can induce about 1 % volume swelling at a temperature range between 400 and 800 °C. However, helium production will not impose a strong swelling effect as temperatures exceed 1000 °C. It has been reported that swelling by helium cavities in the SiC matrix irradiated at 1000 °C ranges from 0.1 − 0.3 % [46]. These results suggest that a fusion blanket based on SiC will have to be designed to accommodate a swelling of 1 %.

3.11.Nano-engineered (NE) nanocrystalline SiC

Some promising paths for improving radiation resistance, such as grain refinement [102], fiber-bonded reinforced composites [4; 103], and increase volume fraction of grain boundaries [20; 104], have been reported. Composites made with the advanced fibers of HNS and the TSA retain dimensional stability and have negligible change in strength up to 10 dpa at 800 °C [105]. SiC composites also show great irradiation resistance under neutron irradiation to doses of 30 to 40 dpa at 300 to 800 °C [50]. However, the irradiation performance of composite is strongly dependent on the degradation of interfacial shear properties [106].

Recently, a self-healing phenomenon in materials during irradiation has been reported. With the use of three atomistic simulation methods, the “loading-unloading” effect in defect-grain boundary interaction in copper from picosecond to microsecond time scales was found [23]. Upon irradiation, the boundary emits interstitials to trigger recombination with vacancies in the bulk. Compared with conventional vacancy diffusion, this recombination mechanism has a lower energy barrier and result in self-healing of the radiation-induced damage. According to this concept, imposing stacking faults (SFs) can enhance the radiation tolerance of SiC.

Recent investigations have shown that NE SiC, which contains high-densities of SFs with nm spacing formed within a nano-sized grain structure, can confine 3-dimensional random point defect migration to a 2-dimensional like movement parallel to the SFs [20]. This result was also demonstrated with observations from *in-situ* TEM of 3C-SiC containing nanolayers of (111) planar defects; two-dimensional migration of radiation-induced point defects, such as interstitials and vacancies, was found between the (111) planar defects [21]. The irradiation-induced defects encounter higher migration barriers across the SFs; thus point defects can either migrate two-dimensionally parallel to the SFs or recombine within a short distance. This nano-layered structure, therefore, enhances the rate of point defect annihilation, leading to improved radiation tolerance of SiC. A previous study [22] has shown an increase in amorphization dose for NE SiC compared to single crystal SiC. Based on DFT calculations, the presence of SFs can make interstitial defects more mobile parallel to the SFs and decreases the binding energy of interstitial-antisite defects, both of which limit defect accumulation [22; 107].

Helium implanted NE SiC is employed in this study to investigate bubble formation under subsequent heavy ion irradiation. Although two-dimensional diffusion is supported by density functional theory calculations [104], the

nucleation and growth of helium bubbles in NE SiC are not well understood. Also, the high-density of SFs with average spacing of 1 to 2 nm could result in significant defect migration and bubble coarsening along grain boundaries, especially in the case of high dose heavy ion irradiated samples. Such defect growth at grain boundaries can impose degradation of mechanical properties.

Therefore, a comparison study of irradiation-induced defect behavior in NE SiC and single crystal SiC is important for improving the understanding of irradiation damage processes and developing radiation tolerant structural materials for future fusion reactors.

Chapter 4. Results and analysis after irradiation

4.1. Single crystal 3C SiC

In the conventional ERDA measurement, forward recoiled helium ions from a 11 MeV O^{4+} ion beam are collected in a Si detector. The depth profile is determined from the energy spectrum of helium ions measured in the Si detector and converted to depth based on energy loss in the mylar film and SiC sample. With a solid angle of 0.0015436 str, and a calibrated silicon energy detector (i.e., E= 3.1178 (keV/ch) * Channel + 85.51 keV), helium depth profile was calculated using the Allegria software [108]. The helium concentration profile in the single crystal 3C SiC determined from the ERDA spectrum is shown in Fig. 4-1. The peak helium concentration is slightly higher than 0.8 % (8000 appm), and helium distribution is slightly shallower than SRIM2012 prediction. However, the experimental result agrees well with the SRIM2012 prediction.

A typical cross-sectional bright field (BF) TEM image from the single crystalline sample implanted to the highest helium fluence (fluence of 1×10^{16} cm^{-2}) is shown in Fig. 4-2. An ordered crystal structure with a few stacking faults is observed; even in the highest helium concentration region, the SiC still remains crystalline.

In the single crystal sample with the highest helium implantation fluence, no bubbles or cavities could be resolved; consequently, the samples with lower helium fluences were reserved for subsequent high temperature heavy-ion irradiation.

In order to understand helium bubble formation and growth mechanisms, the single crystal SiC specimen with the highest helium fluence (1×10^{16} cm^{-2}) was

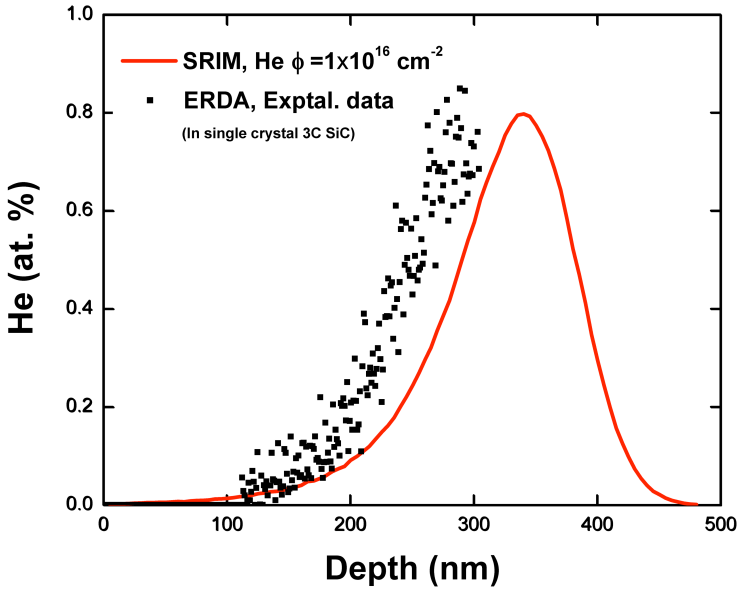

Fig. 4-1 Helium depth profile in single crystal 3C SiC (1×10^{16} cm^{-2}) from the ERDA experiment (dots) and the SRIM2012 prediction (red solid line).

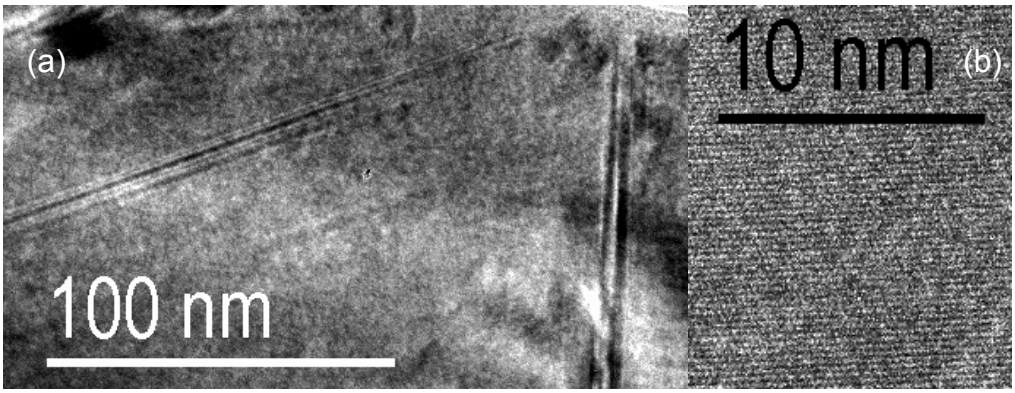

Fig. 4-2 (a) Cross-sectional BF TEM images of single crystal 3C SiC after 65 keV He^+ ion implantation at a fluence of 1×10^{16} cm^{-2} at 277 °C, (b) HRTEM image acquired at 200 kV showing the well-ordered 3C SiC structure.

annealed at 700 °C for 1 hour. Microstructural TEM images are shown in Fig. 4-3. The thermal annealing of the sample implanted with up to 8000 appm helium SiC resulted in the formation of helium platelets and dislocation loops with diameters of about 50 nm. Helium platelets are observed in the specimen at a depth of 370 nm from the surface, which agrees well with the depth of the implanted helium peak predicted by SRIM2012. The helium platelet formation in the 3C SiC is caused by thermal diffusion of helium and residual defects during annealing.

Subsequent heavy-ion irradiation at 700 °C was performed for investigating irradiation-induced gas bubble nucleation and growth. The series of single crystal 3C SiC samples, with different pre-implanted helium fluences, were further irradiated to 10 dpa at 700 °C with 9 MeV Au^{3+} ions. The typical TEM microstructures observed in the single crystal SiC samples with different helium fluences and irradiated to a dose of 10 dpa with 9 MeV Au^{3+} ions at 700 °C are shown in Fig. 4-4; no obvious helium bubbles are observed in the samples with helium peak concentrations from 800 to 8000 appm. Although helium is known to induce blistering and exfoliation at much higher implantation fluences [61], surface blistering was not observed, as expected, for specimens implanted in this study to helium fluences up to 1×10^{16} cm^{-2} (8000 appm at implanted helium peak).

4.2. Nano-engineered (NE) nanocrystalline SiC

Since the helium concentration peak is located at about 330 nm from surface, all TEM micrographs were recorded at a depth of about 330 nm from surface, which is about 170 nm from the film/substrate interface (with the film thickness of about 500 nm). The cross-sectional TEM images are used to determine the size and local density of bubbles; bright field images are recorded when the defocus conditions are at 900 nm of the under defocus value. TEM micrographs of the

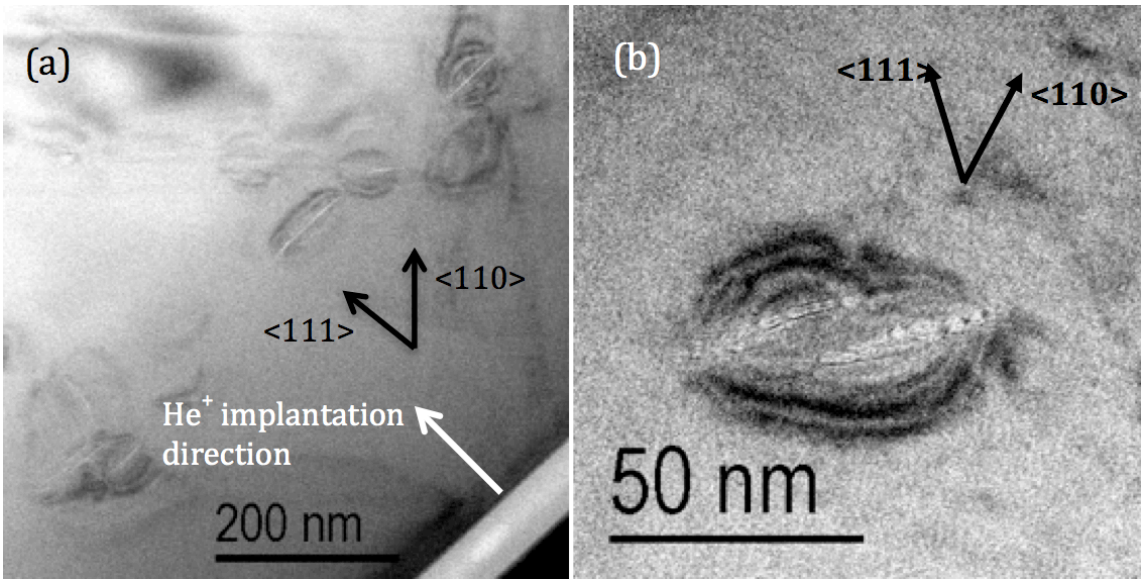

Fig. 4-3 (a) Cross-sectional BF TEM image showing {111} and {110} planar defects in helium-implanted 3C SiC single crystal (1×10^{16} cm^{-2}) following thermal annealing at 700 °C for 1 hour, and (b) Cross-sectional BF HRTEM image acquired at 200 kV showing the planar defects in detail.

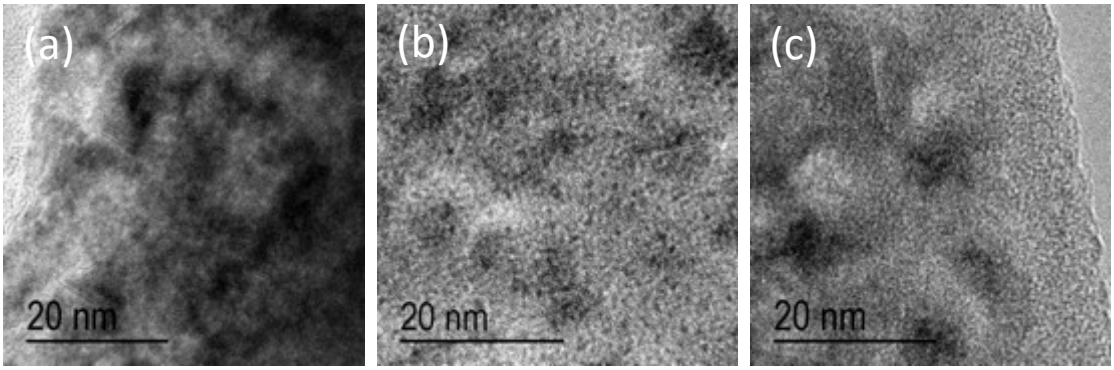

Fig. 4-4 Cross-sectional HRTEM images, taken at 300 to 400 nm from the surface (acquired at 200 kV), for single crystal 3C SiC after irradiation to 10 dpa at 700 °C for pre-implanted helium fluences of (a) 1×10^{15} cm^{-2}, (b) 3×10^{15} cm^{-2}, and (c) 1×10^{16} cm^{-2}.

NE SiC implanted with helium ions are shown in Fig. 4-5. While the high stacking fault densities are clearly observed, the formation of helium bubbles is inconclusive. Compared to the implanted single crystal specimens, the NE SiC contains more defects and provides more nucleation sites that may promote the formation of helium bubbles. Although a bright field through focal images series was recorded, the bubbles were too small (sub-nm) and too few to quantify either size or density with any degree of certainty, and it was only in the as-implanted specimens, with helium fluences of 3×10^{15} cm^{-2} (2400 appm at peak) and higher, that a few sub-nm bubbles were indicated.

Typical TEM micrographs from the helium-implanted NE SiC specimens after annealing for 68 min at 700 °C are shown in Fig. 4-6. In contrast to the helium-implanted single crystal SiC, more evidence for sub-nm helium bubbles was observed in the helium- implanted NE SiC specimens after annealing, but could not be quantified at this stage of bubble evolution. This could support the hypothesis that bubble nucleation is more probable in the NE SiC, but this is still not clearly demonstrated. Similar to the enhanced diffusion of point defects in this NE SiC [20-22], helium may also be more mobile and constrained to two-dimensional migration (parallel to the nano-layered faults), and the two-dimensional diffusion of helium and point defects should enhance nucleation. While helium bubbles are not clearly observable in Fig. 4-6, the high density of stacking faults appears relatively unchanged due to thermal annealing at 700 °C.

To compare the irradiation-induced helium bubble formation behavior in NE SiC with single crystal SiC, the helium implanted NE SiC samples were first irradiated from 10 dpa with 9 MeV Au^{3+} ions at 700 °C. Helium bubbles of different sizes are clearly observed over a wide range of depth, as shown in Fig. 4-7. The average diameters of the helium bubbles are 1.7 ± 0.5 nm, 1.7 ± 0.9 nm and 2.4 ± 1.0 nm, respectively, from the lower helium concentration (1×10^{15} cm^{-2}) to the higher helium concentration (1×10^{16} cm^{-2}).

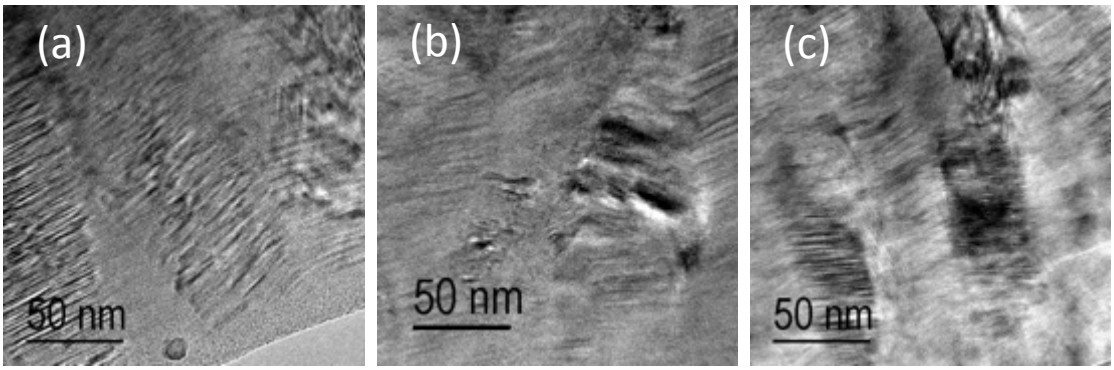

Fig. 4-5 Cross-sectional HRTEM images, taken at 300 to 400 nm from the surface (acquired at 200 kV), for NE SiC after helium implantation fluences of (a) 1×10^{15} cm^{-2}, (b) 3×10^{15} cm^{-2}, and (c) 1×10^{16} cm^{-2}.

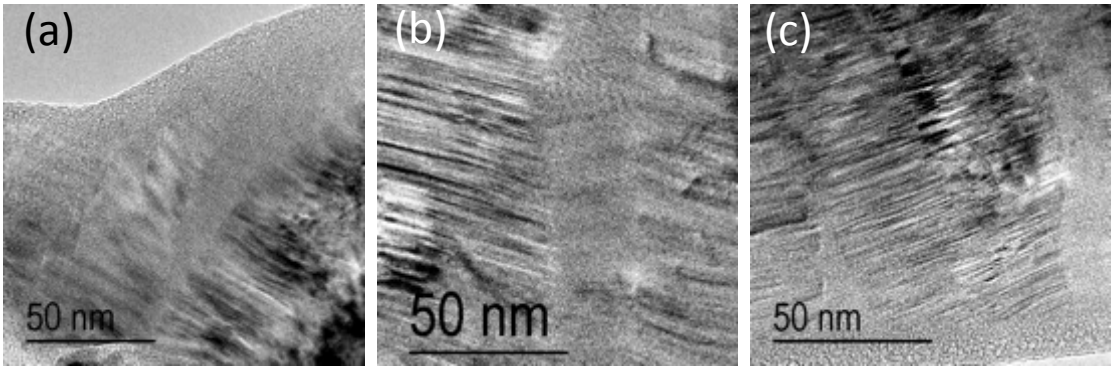

Fig. 4-6 Cross-sectional HRTEM images, taken at 300 to 400 nm from the surface (acquired at 200 kV), for NE SiC after 700 °C annealing for 68 minutes for helium implantation fluences of (a) 1×10^{15} cm^{-2}, (b) 3×10^{15} cm^{-2}, and (c) 1×10^{16} cm^{-2}.

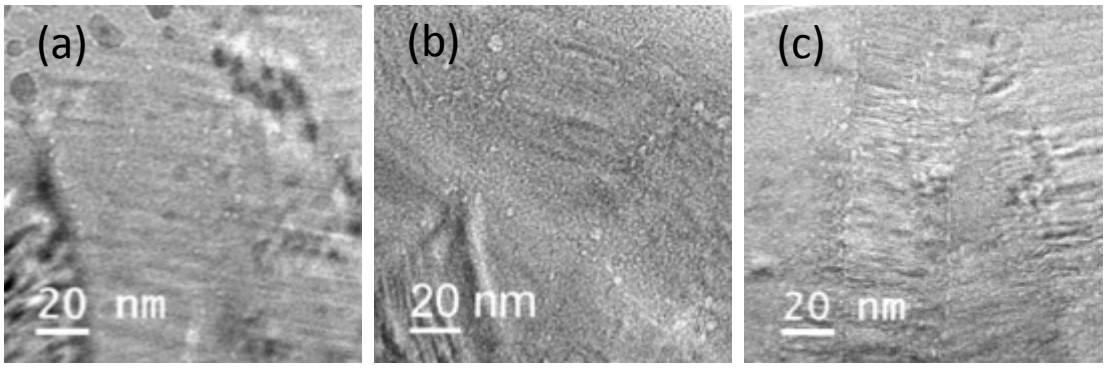

Fig. 4-7 Cross-sectional HRTEM images, taken at 300 to 400 nm from the surface (acquired at 200 kV), for NE SiC after Au^{3+} ions irradiation to 10 dpa at 700 °C for helium fluence of (a) 1×10^{15} cm^{-2}, (b) 3×10^{15} cm^{-2}, and (c) 1×10^{16} cm^{-2}.

Following the subsequent 9 MeV Au^{3+} irradiation to a dose of 20 dpa, helium bubble formation could be observed in specimens with helium fluences of 1×10^{15} cm^{-2} (800 appm at peak) and higher, as shown in Fig. 4-8. The average diameters of the helium bubbles are 1.7±0.4 nm, and 1.8±0.4 nm for helium fluences of 1×10^{15} and 3×10^{15} cm^{-2}, respectively. Bubble precipitation and growth are driven by the continuous production of irradiation-induced defects. The areal number density of helium bubble slightly decreased as the helium concentration increased.

As shown in Fig. 4-9, helium bubble formation is observed in all specimens with different helium concentrations after further Au^{3+} ions irradiation to a dose of 30 dpa. The average diameters of the helium bubbles are 1.7±0.4 nm, 1.8±0.4 nm and 2.4±0.7 nm, respectively, from the lowest (1×10^{15} cm^{-2}), medium (3×10^{15} cm^{-2}), and highest helium concentration (1×10^{16} cm^{-2}). Due to the preferential helium bubble distribution in the NE SiC along grain boundaries, the density is not uniform enough to calculate the volume swelling; however, the estimated bubble volume swelling is on the order of less than 0.05 %.

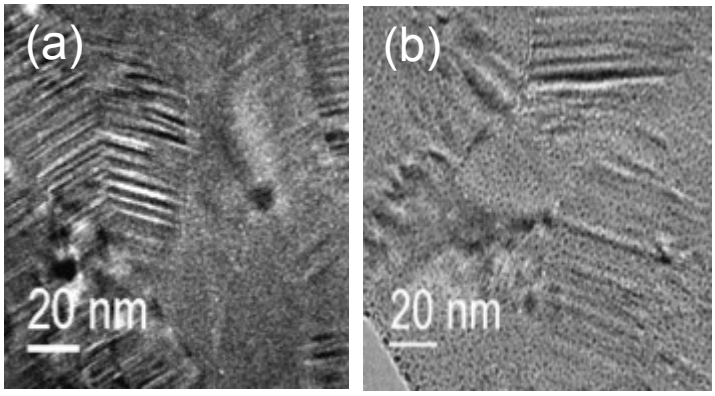

Fig. 4-8 Cross-sectional HRTEM images, taken at 300 to 400 nm from the surface (acquired at 200 kV), for NE SiC after Au^{3+} ions irradiation to 20 dpa at 700 °C for helium fluence of (a) 1×10^{15} cm^{-2} and (b) 3×10^{15} cm^{-2}.

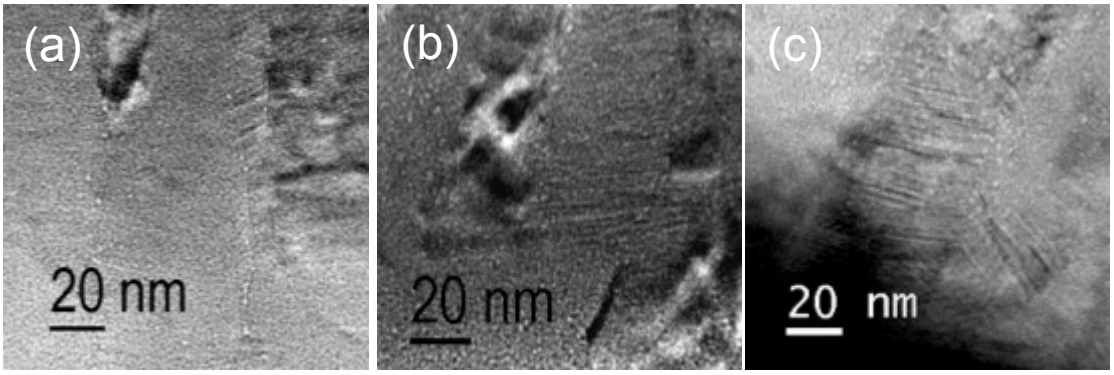

Fig. 4-9 Cross-sectional HRTEM images, taken at 300 to 400 nm from the surface (acquired at 200 kV), for NE SiC after Au^{3+} ions irradiation to 30 dpa at 700 °C for helium fluence of (a) 1×10^{15} cm^{-2}, (b) 3×10^{15} cm^{-2}, and (c) 1×10^{16} cm^{-2}.

Average bubbles sizes and densities are summarized in Table 4-1 and 4-2. It was observed that in low dose ion-irradiated specimen (10 dpa/ 1×10^{16} helium ions*cm^{-2}), smaller helium bubbles with an average diameter of 1.7 nm are randomly distributed within the grain; larger bubbles with an average diameter of 2.6 nm are formed along the grain boundaries. While the location-dependent size divergence of the same specimen was not obviously observed under high dose ion irradiation. Only slight differences can be found after 30 dpa ion irradiation (with average size of 2.3 nm within grain and 2.5 nm at grain boundaries). No obvious helium bubbles are observed outside the helium-implanted region, which confirms that radiation-induced helium migration is limited perpendicular to the SF planes but readily migrate two-dimensionally parallel to the SFs.

It is shown in Fig. 4-10 (a) that the deviation of the bubble diameter is reduced as the damage level is increased. However, the increase in bubble density with increasing damage level (as shown in Fig. 4-10 (b)), which suggests that both nucleation and growth proceed simultaneously at 700 °C under heavy ion-irradiation. With the same irradiation damage level, the samples with the highest helium concentration exhibit the lowest areal bubble number density. This demonstrates that helium atoms keep nucleating and migrating in preferential sites in NE SiC.

Helium bubbles at grain boundaries and within the grains are observed in the Au-irradiated specimens for all helium concentrations. These results demonstrate that helium can migrate and nucleate bubbles at preferential sites in the NE SiC. Most of the bubbles are observed at the grain boundaries since grain boundaries can act as strong sinks for both the implanted helium and irradiation-induced defects. The bubbles at grain boundaries are larger in size (varying from 1 to 5 nm) compared with the average size within the grains.

Table 4-1 Averaged helium bubble diameters under different heavy ion irradiation doses in NE SiC.

He Fluence (cm^{-2})	He^+ implanted + subsequent Au^{3+} post irradiation 700 °C **(10 dpa) [109]**	He^+ implanted + subsequent Au^{3+} post irradiation 700 °C **(20 dpa)**	He^+ implanted + subsequent Au^{3+} post irradiation 700 °C **(30 dpa)**
	Bubble averaged size (nm)		
1e15	1.7 ± 0.5	1.7 ± 0.4	1.7 ± 0.4
3e15	1.7 ± 0.9	1.8 ± 0.4	1.8 ± 0.4
1e16	2.4 ± 1.0	Unavailable	2.4 ± 0.7

Table 4-2 Helium bubble number densities under different heavy ion irradiation doses in NE SiC

He Fluence (cm^{-2})	He^+ implanted + subsequent Au^{3+} post irradiation 700 °C **(10 dpa) [109]**	He^+ implanted + subsequent Au^{3+} post irradiation 700 °C **(20 dpa)**	He^+ implanted + subsequent Au^{3+} post irradiation 700 °C **(30 dpa)**
	Number density ($10^{-3}/nm^3$)		
1e15	0.7	3.34	5.35
3e15	0.66	2.77	3.12
1e16	0.58	Unavailable	2.08

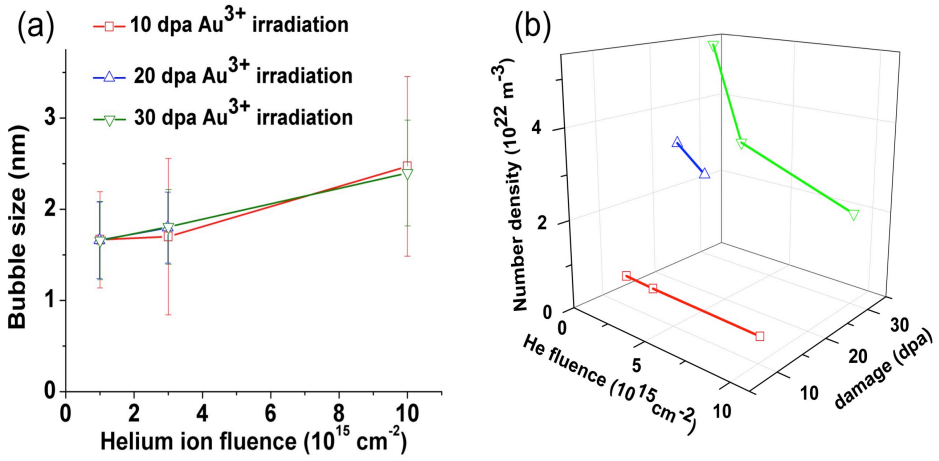

Fig. 4-10 Averaged helium bubble size (a) and number density (b) of NE SiC after Au^{3+} ions irradiation from 0 dpa to 30 dpa at 700 °C with He fluences from 1 x 10^{15} to 1 x 10^{16} cm^{-2}.

During irradiation, the migration and interaction of mobile defects and gas atoms with each other or with immobile defects can lead to microstructural evolution, such as the nucleation and growth of bubbles. Thus, increasing numbers of visible helium bubbles are observed in the NE SiC within the grains and at grain boundaries as the damage level increased. Although the damage level went as high as 30 dpa, the helium bubbles did not grow to a noticeable extent. However, the helium number density increased significantly, from 4 to 10 times, as the damage level increased. This suggests that the evolution of helium bubbles is still undergoing nucleation and not growth, which suggests a long-term incubation process for helium bubbles under these irradiation conditions.

The number density of helium bubble under various irradiation conditions are summarized and discussed in Ch 6. It was found that the mean helium bubble diameter in the NE SiC is lower than other values reported in the literature [46; 71; 75; 87; 89; 90; 110]. It's also worth mentioning that those other studies in the

literature were investigating bubble formation at higher temperatures and helium concentrations than in this study.

As reported in previous studies, hydrogen enhances bubble nucleation and inhibits bubble growth in SiC, which has been validated when comparing dual and triple ion beam irradiation results [89]. At 700 °C in the present study, helium bubbles are found to have a smaller average size in the NE SiC than in SiC composites irradiated at higher temperatures, although the number densities are comparable. For SiC composites irradiated at 800 °C, bubble growth is clearly observed as damage increases from 10 to 100 dpa. Significant coalescence of bubbles into larger size bubbles is only reported for irradiation temperatures above 1000 °C, which can also lead to a decrease in the number density.

ToF-ERDA measurements

To determine the helium depth distribution, Ni and Ti ion beams were employed for ToF-ERDA measurements. Helium depth distributions in the NE SiC before/after ion irradiation acquired from ToF-ERDA are shown in Fig. 4-11. The ToF-ERDA results suggest that the helium distribution is slightly shallower to the surface and peak concentration is about 10 % higher than SRIM2012 prediction, which agrees well with the results from conventional ERDA measurement of the helium-implanted single crystal SiC. Although the free surface and film/substrate interface act as sinks for helium, helium atoms were only observed in a depth range of about ±50 nm from the depth of the injected helium peak. No broadening or redistribution of helium depth profile was observed along the ion path. This suggests that the helium atom diffusion is insignificant perpendicular to the stacking faults, and short range migration may only occur parallel to the SFs. The enhanced radiation tolerance and gas atom confinement in the NE SiC film under ion-irradiation to 30 dpa may be attributed to the high density of SFs.

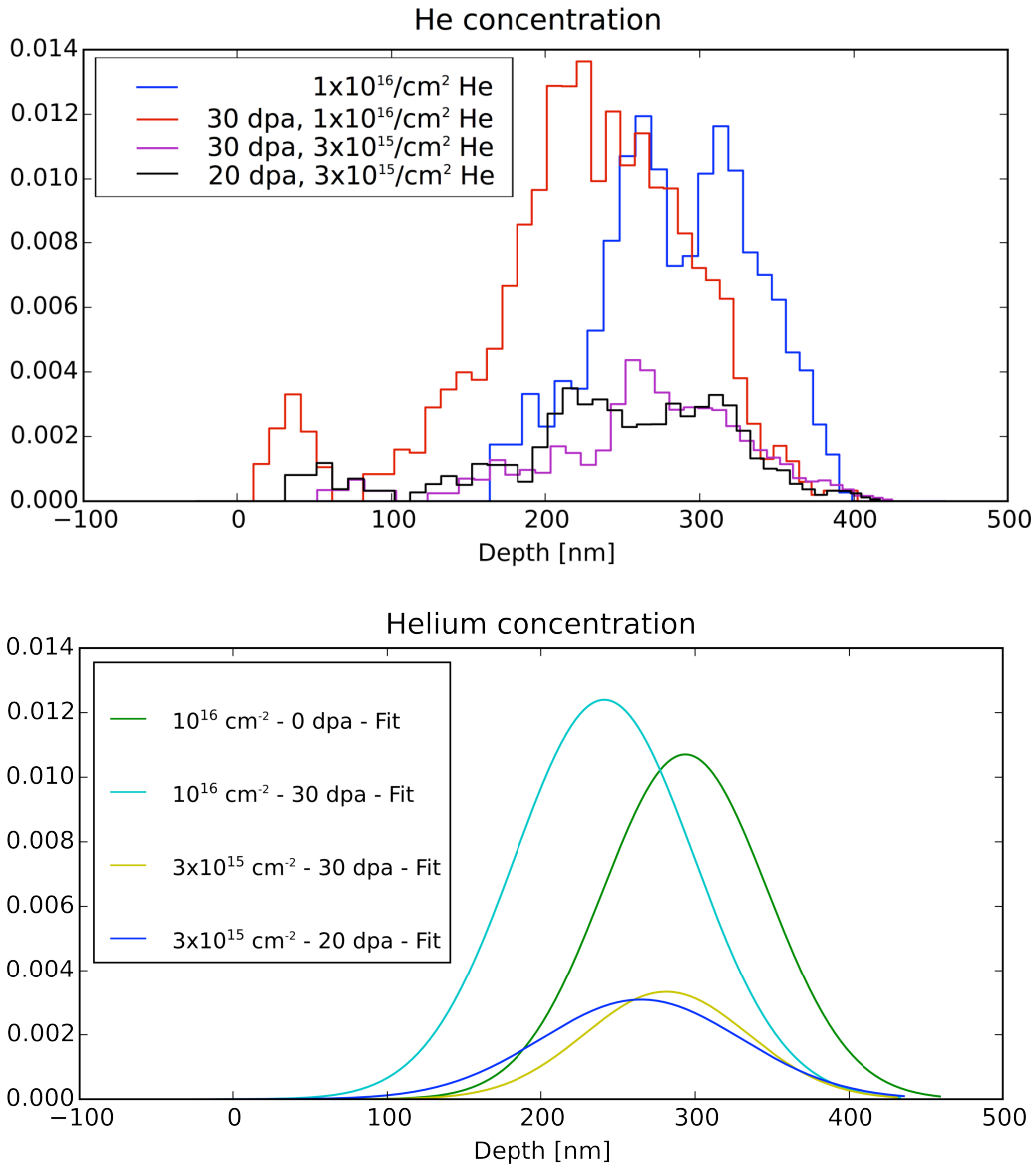

Fig. 4-11 (a) Raw data of helium depth distribution from ToF-ERDA measurement. (b) Normalized helium depth distribution in NE SiC before/after irradiation from 20 to 30 dpa at 700 °C with helium fluence of 3×10^{15} cm^{-2} and 1×10^{16} cm^{-2}.

4.3. Post *in-situ* 1 MeV Kr^{2+} irradiation on NE SiC

Cross-sectional TEM revealed the presence of nanometer-sized helium bubbles in the NE SiC after Au irradiation, but only over the depth corresponding to the implanted helium, indicating minimal migration of helium across the stacking faults. Additional irradiations at 700 °C to 30 dpa revealed no significant increase in helium bubble size, but an increase in bubble density, as illustrated in Fig. 4-10, suggesting a long bubble incubation period at 700 °C.

To better understand the evolution of helium bubbles under irradiation at higher temperatures, *in-situ* irradiation experiments using the Intermediate Voltage Electron Microscope (IVEM)-Tandem facility at Argonne National Laboratory are performed. Prior to the *in-situ* irradiation experiment, the NE SiC thin films were first implanted at 277 °C with helium to a peak concentration of 0.8 at. % (i.e. fluence of 1×10^{16} ions cm^{-2}). These helium-implanted specimens were then subsequently irradiated with heavy ion (9 MeV Au^{3+} ions) at 700 °C to an ion fluence of 2.3×10^{16} ions cm^{-2} (30 dpa) to produce a relatively flat-damage profile at the helium peak region (depth of 270 to 390 nm). The cross-sectional TEM samples were mounted on Moly TEM grids, and TEM transparency and presence of helium bubbles were confirmed beforehand. Using the SRIM full-cascade simulations (version 2012) [24], the irradiation dose in displacements per atom (dpa) was calculated assuming a sample density of 3.21 g cm^{-3} and threshold displacement energies of 20 and 35 eV for the C and Si atoms, respectively [28]. The depth profile of the atomic displacements from irradiation with 1 MeV Kr^{2+} ions in the NE SiC is shown in Fig. 4-12. It is worth noting that less than 0.01 at. % of the irradiated Kr ions are retained in the TEM specimen of 100 nm thickness.

In these *in-situ* irradiation experiments, the irradiations of the electron-transparent specimens were conducted using 1 MeV Kr^{2+} ions at 350 and 800 °C

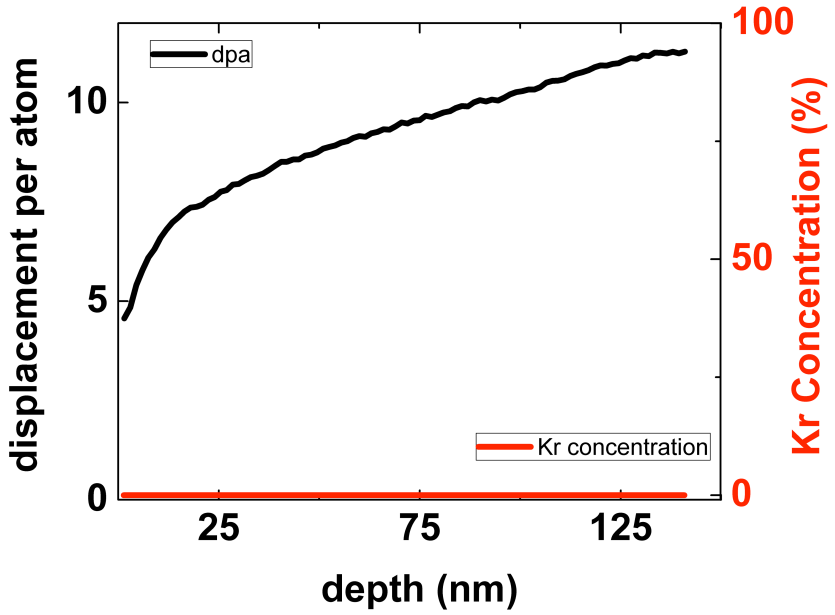

Fig. 4-12 SRIM simulations of the irradiation damage prediction (1 MeV Kr irradiation with a dose of 10 dpa) and Kr concentration (below 0.1 at. %) in the NE SiC TEM specimen.

to ion fluences up to 2×10^{16} (20 dpa) to produce a relatively flat-damage profile within the TEM specimen. The specimens were characterized using a Hitachi 9000 high-resolution transmission-electron-microscope (HRTEM) operating at 300 kV. This approach provides a reliable comparison of helium evolution in NE SiC under irradiation at different temperatures.

The energy of the ion beam was chosen such that the damage energy deposited into the NE SiC film has a smooth gradient, while minimizing the Kr concentration in the TEM specimen. The specimens were irradiated with an incident angle of 15° from the specimen normal. The ion flux was kept constant (about 7×10^{11} $cm^{-2}s^{-1}$) during the Kr irradiation, and ion dosimetry was measured using Faraday cup in the microscope below the specimen. The temperature was controlled

using the heating system at the TEM sample holder. Micrograph images were collected using Gatan Orius 1000 digital camera. Helium bubbles are determined via through focus imaging.

Experimental results and analysis

Microstructure prior to *in-situ* irradiation

Before Kr irradiation, the average diameter of the pre-existed helium bubbles in the NE SiC sample was 2.4±0.7 nm, with a peak helium concentration of 0.8 at. % (1×10^{16} ions cm^{-2}). The number density of helium bubbles was $2.08\times10^{22}/m^3$. Because of the preferential bubble formation at grain boundaries, the average bubble diameter at grain boundaries (2.6 nm) was about 1.5 times larger than inside the grain (1.7 nm).

Helium bubble stability under irradiation at 350 °C

The NE SiC specimen was first irradiated to 5 dpa at 350 °C. From the through focus imaging (not shown in figure), it was concluded that there was no obvious microstructural evolution. The size and shape of all the pre-existed helium bubbles remained the same. Also no sputtering of the edges of the specimen was observed.

Helium bubble stability under irradiation at 800 °C

Although bubble nucleation and growth can be driven by the continuous production of irradiation-induced defects, in this study, significant bubble growth was not observed. Also no dislocation loops were observed even after Kr irradiation to 20 dpa.

The microstructural evolution in the NE SiC induced by *in-situ* Kr irradiation is shown in Fig. 4-13. All TEM micrographs were recorded with the same defocus value (900 nm under focus). As shown in Fig. 4-13, following the 1 MeV Kr^{2+} irradiation process to a dose of 15 dpa, no obvious bubble migration or coalescence was observed. Although the number density of bubbles gradually decreased with dose, the average bubble diameter remained almost the same value, below 10 dpa. However, above 10 dpa, a majority of the helium bubbles decreased in size, while keeping a spherical bubble shape. In addition to the decrease of bubble diameter, some large bubbles split into smaller bubbles, which contributed to the overall decrease in average bubble diameter. Several different forms of bubble evolution are shown in Fig. 4-14. Only a small number of bubbles exhibited a small but discernable growth under irradiation, as shown in Fig. 4-14. Compared with bubble shrinkage, bubble growth is rare, which is in contrast to what is observed for bulk irradiation.

The number density and average diameter of helium bubbles under continuous Kr irradiation are summarized in Table 4-3 and Fig. 4-15. The number density of the helium bubbles continuously decreased to one-third of its starting value after Kr irradiation to a dose of 15 dpa. While the average bubble shrinkage only occurred as damage level exceeded 10 dpa. The average bubble diameter was found to be 1.56±0.48 nm at a dose of 15 dpa, which is about two-third of its original size. The normalized helium bubble size distributions in the NE SiC from *in-situ* irradiation are summarized in Fig. 4-16. A Gaussian fit (solid line) was employed for the bubble size distribution. Small bubbles with sub-nano size (below 1 nm) were observed only after irradiation to a dose of 15 dpa. The sub-nano size is shown by a dash line due to the resolution limitations of the TEM measurements. This dramatic decrease in bubble size suggests that a significant number of helium atom are ballistically knocked out of the bubbles. In addition, the rate for helium atom re-trapping into bubbles is strongly decreased due to helium loss to the surface to the TEM samples.

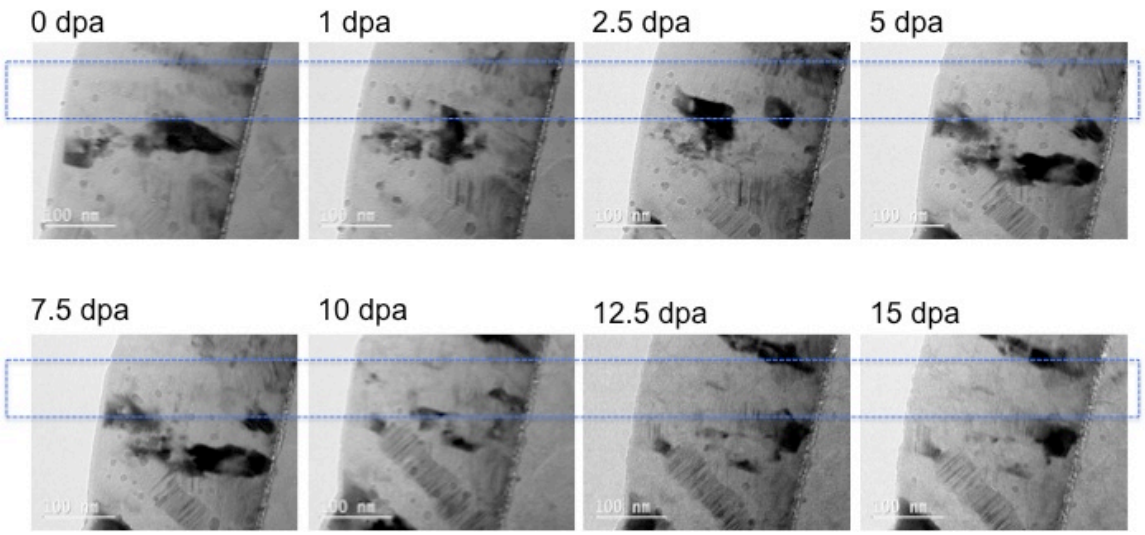

Fig. 4-13. A series of under-focused BF TEM images (acquired at 300 kV) of NE SiC during *in-situ* Kr^{2+} irradiation at 800 °C. With the previous processes of pre-helium-implantation (fluence of $1\times10^{16}\,cm^{-2}$) and subsequent Au-irradiation (30 dpa), the existence of nano-sized helium bubbles can be observed at the depth range of 300 to 400 nm from the surface in NE SiC before *in-situ* Kr^{2+} irradiation. However, the bubble shrank and disappeared as the damage dose of Kr^{2+} irradiation exceeded 10 dpa. All photos were taken with the same defocus value (900 nm under focus).

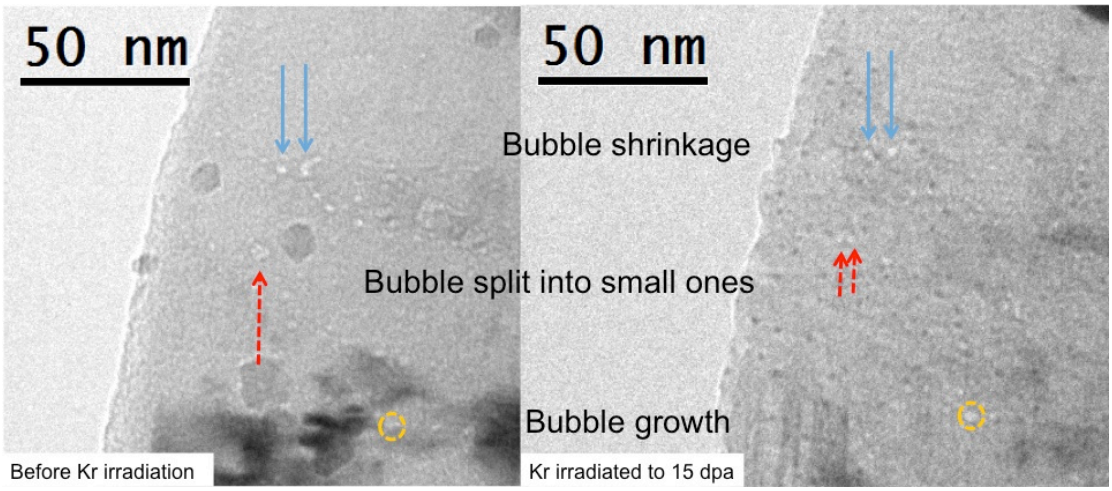

Fig. 4-14. Micrographs of helium bubble evolution before/after irradiation. Bubble shrinkage, break and growth were observed and indicated with arrow line, dash arrow line and circle, respectively.

Table 4-3 Averaged values of helium bubble diameter and number density under different heavy ion irradiation doses in NE SiC.

	Bubble Diameter (nm)	Density ($10^{22}/m^3$)
1e16 He 30 dpa Au irradiation at 700 °C	2.4 ± 0.7	2.08
1e16 He 30 dpa Au irradiation at 700 °C Plus Kr irradiation to 1 dpa at 800 °C	2.36 ± 0.75	1.68
1e16 He 30 dpa Au irradiation at 700 °C Plus Kr irradiation to 2.5 dpa at 800 °C	2.37 ± 0.79	1.32
1e16 He 30 dpa Au irradiation at 700 °C Plus Kr irradiation to 5 dpa at 800 °C	2.38 ± 0.79	1.07
1e16 He 30 dpa Au irradiation at 700 °C Plus Kr irradiation to 10 dpa at 800 °C	2.35 ± 0.80	0.92
1e16 He 30 dpa Au irradiation at 700 °C Plus Kr irradiation to 12.5 dpa at 800 °C	2.05 ± 0.62	0.89
1e16 He 30 dpa Au irradiation at 700 °C Plus Kr irradiation to 15 dpa at 800 °C	1.56 ± 0.48	0.71

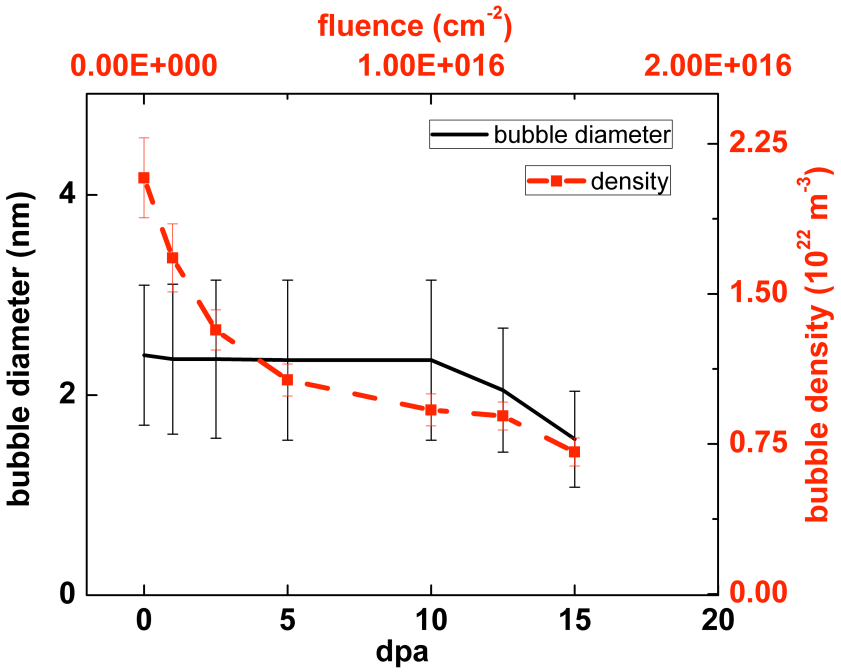

Fig. 4-15 Averaged helium bubble size and number density of NE SiC after Kr $^{2+}$ ions irradiation from 1 dpa to 15 dpa at 800 °C with He fluences of 1×10^{16} ions cm^{-2}.

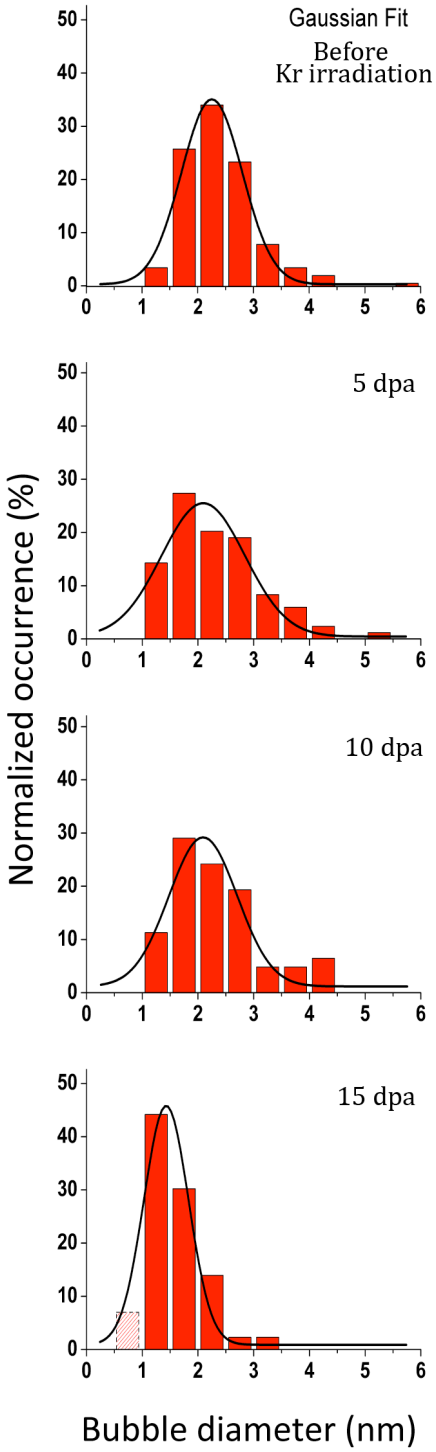

Fig. 4-16. Normalized bubble size distribution in NE SiC after irradiation at 800 °C, the average diameter of helium bubble decreases as damage increases.

Stacking fault stability under irradiation

Thanks to the enhanced defect recombination rate, it was previously reported that the NE SiC is more radiation tolerant and has shown a superior structural stability under irradiation [20-22]. At 800 °C under Kr irradiation, however, besides the bubble dissolution and helium loss, SFs annihilation in the TEM specimen under irradiation was also observed. The contrast of the nano-layered SF structure diminished as damage approached 20 dpa, as shown in Fig. 4-17 and 4-18. This diminished contrast indicates that the SF layers are recovering within the TEM specimen with total thickness less than 150 nm.

Migration Mechanism

Although the peak swelling temperature in the NE SiC under these irradiation conditions is still unknown, the decrease in size and loss of bubbles can be understood as ballistic dissolution process combined with helium outgassing during irradiation. As illustrated in Fig. 4-19, the free surfaces of the TEM sample, which act as sinks, may attract defects during high temperature irradiation. Therefore, the *in-situ* irradiation can induce helium migration and release of helium atoms close to surface.

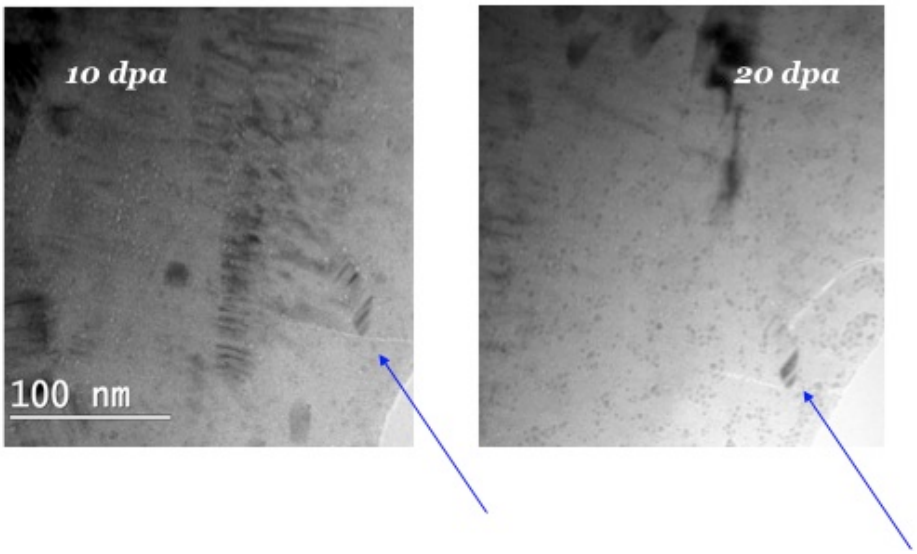

Fig. 4-17 In-situ Kr irradiation induced stacking fault diminishing in TEM specimen as damage goes up to 20 dpa.

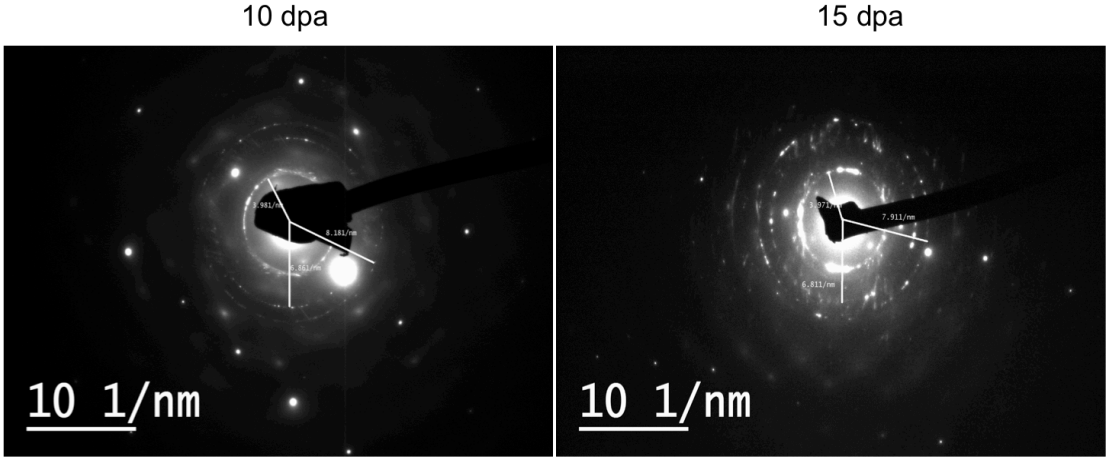

Fig. 4-18 *In-situ* Kr irradiation induced formation of extra spots in diffraction pattern, suggesting the SF layers are recovering.

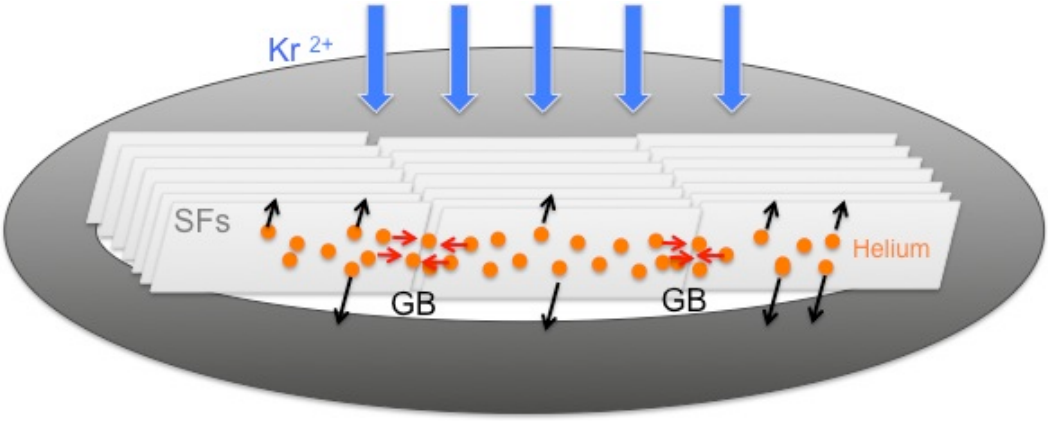

Fig. 4-19 *In-situ* Kr irradiation induced defect migration in TEM specimen. Although defect migration is confined within SF layers, due to the existence of free surfaces in TEM sample, instead of being trapped by existed bubbles at grain boundaries, helium interstitials close to surface may diffuse toward the surface and result in the helium release.

Chapter 5. Quantify the helium distribution by electron energy loss spectroscopy (EELS)

5.1. Electron Energy Loss Spectroscopy (EELS)

By measuring the change in kinetic energy of electrons after interacting with the specimen, electron-energy-loss spectroscopy can provide both chemical information and fine structure information related to the electronic densities of states. Since the scanning spot can be minimized to a fairly small area (i.e., about 2 x 2 nm^2 in the LIBRA 200F MC-HT) in STEM mode, it's a good way for approaching local properties in nano-scale. This approach includes investigating chemical composition, mechanical and electronic properties (such as band-gap). It was previously reported that a procedure for measuring the density of He in nanometre-sized bubbles using the relation between He density and energy shift from electron-energy-loss spectroscopy is validated in several materials [2; 4; 39; 40; 111-113].

5.2. Electron shift and helium density

It's well known that radiation damage from fast neutrons and the production of helium and hydrogen gas atoms from nuclear reactions can induce gas bubble formation in SiC. However, measurement of helium distribution has been restricted due to the probing limitation of traditional TEM.

An approach combining TEM observation and EELS is demonstrated to determine the concentration and pressure of nano-size helium bubble in NE SiC.

In the current work, with the EELS approach, the relation of chemical shift of the helium K-edge with helium atom density in bubbles of a few nanometer in diameter is investigated in NE SiC. In the helium implanted NE SiC specimens, the energy shift of the helium (1s-2p) peak was measured as a function of helium atom density.

The relation is also compared with previous results from helium-implanted alloys. Formation and distribution of helium-gas bubbles associated with stacking faults can be understood via the results.

5.3. Helium K edge energy shift

It was previously reported that because of the overlapping of the wave function of the neighboring helium atoms, a blue shift of less than 1 eV from the helium free atom value of 21.218 eV (Kuhn 1962) [114] can be observed in liquid helium (Surko et at. 1969) [115]. At room temperature, using a model based on helium atom pair potentials, a linear relationship between energy shift (ΔE) and helium density (n) in aluminum has been derived by Lucas *et al*. [2], as shown in Fig. 5-1, given by

$$\Delta E(eV) = C_n n - 0.15 = 31n\left(A^{\circ -3}\right) - 0.15$$

On-the-other-hand, it was also calculated by Chen *et al*. [4] that the energy shift as a function of helium bubble radii can be expressed as a linear relationship, shown in Fig. 5-2, and given by

$$\Delta E(eV) = (0.18 \pm 0.02) + (10.26 \pm 0.32) \times (1/r(A))$$

Therefore, it has been shown that EELS can be used to determine the number density of helium atoms in bubbles by measuring the size of bubble and the shift

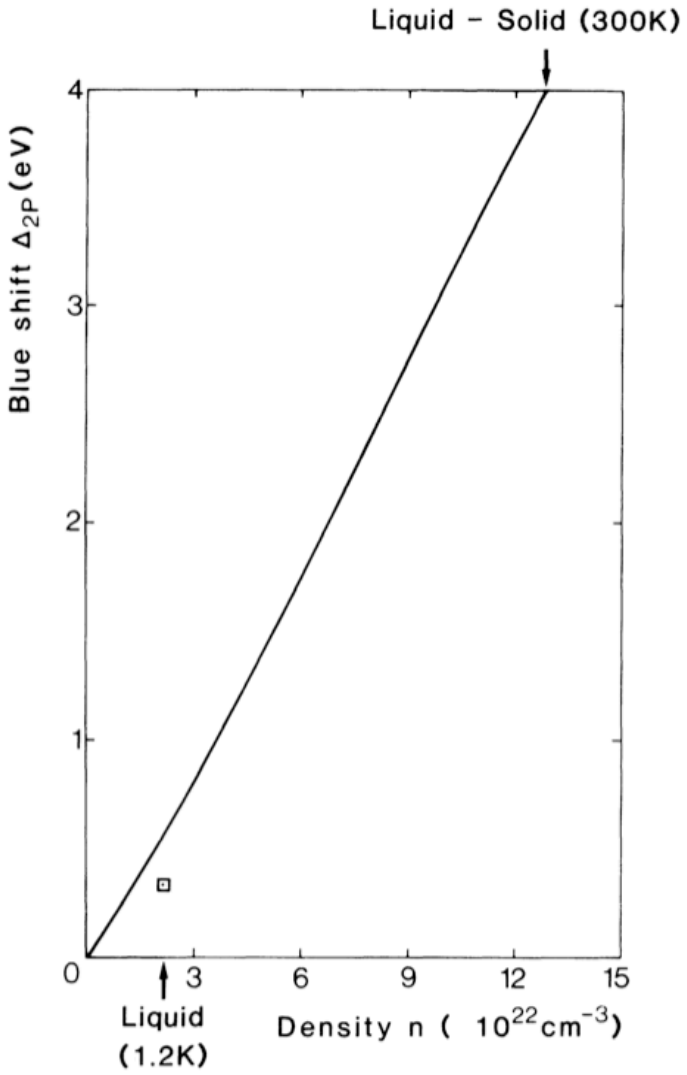

Fig. 5-1. Linear relationship between Blue-shift and helium gas density at room temperature, derived by Lucas *et al* [2].

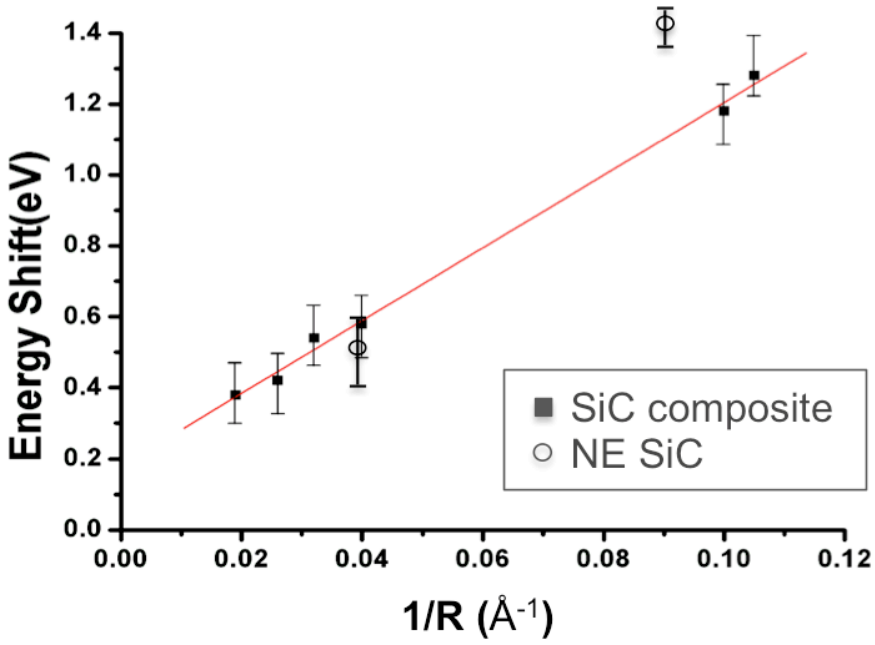

Fig. 5-2. The relationship between Blue-shift and helium bubble size. Amount of energy shift of He K-edge can be expressed as a function of 1/R. From the results reported by Chen *et al.* [4], the energy shift and inverse radius exhibit a linear relationship.

electron microscope (STEM) with an electron beam of sub-nm in size, which can be focused on individual bubbles with different size. In this work, helium bubbles with a diameter range from 2 to 5 nm were investigated using EELS. As illustrated in Fig. 5-3, a spectrum with a shift in the helium K edge peak is observed; the energy shift increases with decreasing bubble size. Data from this work (NE SiC) are shown as circular data points in Fig 5-2. These data are in good agreement with the previous results for helium bubbles in SiC composite.

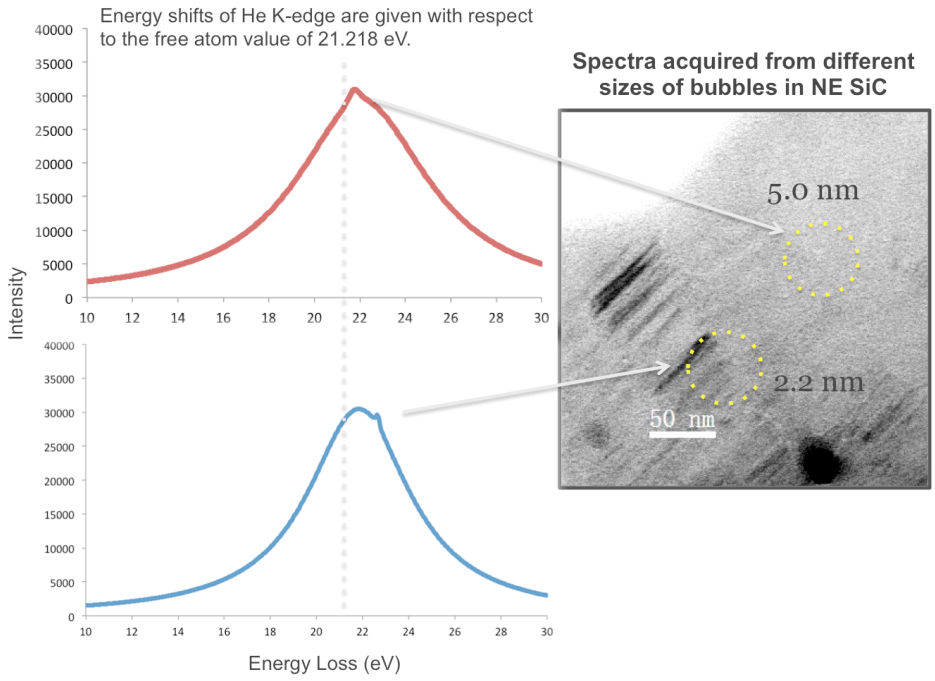

Fig. 5-3. Energy shift of He K-edge can be observed in spectra from individual bubbles. Data of energy shift and bubble size from irradiated NE SiC specimen were plotted in Fig. 5-2 with circles.

5.4. Density calculation

From the above equations, the density (*n*) of helium in bubbles of a given size can be estimated from both the energy shift and bubble radii. By assuming a

spherical shape for the bubbles, the concentration of helium in the bubbles can be calculated from the expression:

$$\text{Density of Helium}\,(N)\,(1/cm^3) = D \times (\frac{4}{3}\pi r^3) \times n$$

where *D* is the number density of bubbles and *n* is the helium atom density of a bubble.

In addition, the implanted helium density can be estimated, since the fluence (*F*) is already known, and the full breadth of the helium distribution (*L*) in SiC can be measured from ERDA experiments.

$$\text{Implanted Helium}\,(N_0)\,(1/cm^3) = F(ions/cm^2)/L$$

The percentage of helium atoms trapped in the bubbles can thus be determined by comparing the values of *N* and N_0:

$$\text{Helium \% in Bubbles} = N/N_0$$

Table 5-1 shows the results from different irradiation condition with damage levels from 10 to 100 dpa and temperatures from 700 to 1000 °C. Our results at 700 °C indicate that very few helium atoms are trapped into bubbles, which agrees well with an ongoing long-term incubation process at 700 °C. This phenomenon indicates that without the aid of thermal driven diffusion, bubble formation and growth is relatively low at this temperature. Also because of hydrogen enhanced bubble nucleation, significant bubble coarsening is only expected under dual ion beam irradiation [89].

Table 5-1. The percentage of helium atoms trapped in the bubbles under different ion irradiation conditions in NE SiC and SiC composites.

Irradiation condition	Bubble Radii (nm)	N (#/cm^3)	N_0 (#/cm^3)	He %
700 °C/ He & Au (8000 appm/ 10 dpa)	1.2±0.45	9.03×10^{17}	4×10^{20}	0.23
700 °C/ He & Au (8000 appm/ 30 dpa)	1.2±0.35	5.75×10^{18}	5×10^{20}	1.2
800 °C/ He & Si (15000 appm/ 100 dpa)	4.25±1.60	3.67×10^{19}	1.44×10^{20}	25.5
800 °C/ He & H & Si (1500 appm/ 600appm/ 10 dpa)	1.19±0.18	4.93×10^{19}	1.22×10^{20}	40.4
1000 °C/ He & Si (15000 appm/ 100 dpa)	2.87±1.21	9.63×10^{18}	7.5×10^{19}	100
	10.8±3.3	8.98×10^{19}		
1000 °C/ He & H & Si (1500 appm/ 600appm/ 10 dpa)	1.81±0.47	1.04×10^{20}	6.4×10^{19}	100

5.5. Pressure of helium bubbles

In this work, a non-linear relationship between energy shift and pressure at room temperature, as reported by Mills *et al*. [3], and illustrated in Fig. 5-4, is employed to determine the pressure within individual helium bubble. In the NE SiC specimen, helium densities of 50 and 21.3 nm^{-3} were observed in bubbles with diameters of 2.2 and 5 nm, respectively. According to Fig. 5-4, the pressure within the helium bubbles are 0.68 GPa (small bubble) and 0.12 GPa (large bubble). According to the density of liquid He (21.8 nm^{-3}) reported by Donnelly *et al.* [116; 117], most of the helium within bubbles in NE SiC may be in the solid or liquid phase. The mechanism for bubble growth with a pressure decrease is because of vacancy absorption and migration or coalescence of bubbles, which can only occur when vacancies become sufficiently mobile [40].

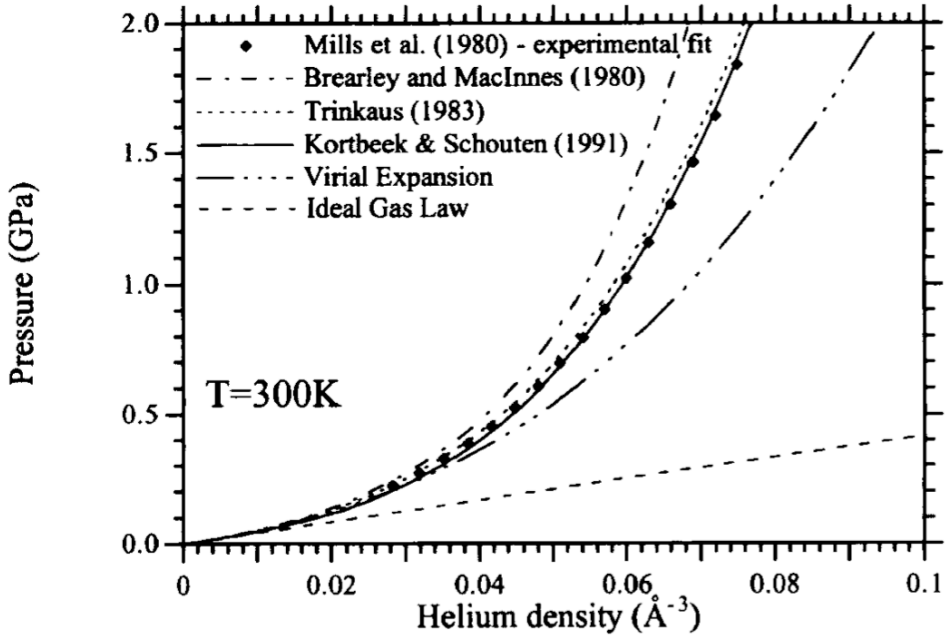

Fig. 5-4. The relationship between gas bubble pressure and helium density. Calculation from the most appropriate equation of state are compared with experimental data from Mills *et al.* (1980) at T = 300 K [3].

Chapter 6. Disscussion

6.1. Single crystal 3C SiC behavior

Studies of helium behavior in SiC single crystals (4H and 6H) following room temperature implantation and annealing have indicated that bubbles, platelets or even planar clusters are observed to form only at higher temperatures (mostly higher than 800 °C) or above a certain threshold helium concentration (i.e. 600 appm at 1427 °C) [67; 76]. Our observation for He^+ implanted 3C SiC, shown in Fig. 4-2, is in good agreement with Zinkle's results [61] who reported that, at room temperature and 650 °C, the threshold helium concentrations for bubble formation in SiC are 1.7 at. % (17000 appm) and 2 at. % (20000 appm), respectively. Hence, no helium bubbles are expected in the single crystal 3C SiC implanted with helium to a fluence of 1×10^{16} cm^{-2} (~ 8000 appm at implanted helium peak) at 277 °C. The irradiation-induced damage in the 3C SiC did not have a pronounced effect on the formation of helium bubbles, although a low density of large dislocation loops (~50 nm diameter) are observed in the mid-range region at about 300 nm from the implantation surface (Fig. 4-4). Figure 4-3 shows the microstructure of SiC in the helium peak region after one hour thermal annealing at 700 °C. Cavities or bubbles observed in the helium implanted region are highly localized in this region and preferentially associated with dislocation loops lying on the {1 1 1} and {1 1 0} habit planes. The cavities appear as platelets coinciding with the loops. Hence, the annealing temperature of 700 °C is insufficient for longer-range helium diffusion, but local precipitation is possible. This is in agreement with Miro *et al*. [118], who found thermally-activated helium migration in single crystal SiC only occurs above 1100 °C.

6.2. Nano-engineered (NE) SiC behavior

We have investigated phase stability and helium bubble formation for an irradiation dose from 10 to 30 dpa at 700 °C. In contrast to the behavior in single crystal 3C SiC, helium bubbles with measurable sizes are formed in high-temperature irradiated NE SiC. The results indicate that the crystallinity and SF structure exhibit great irradiation resistance at high temperature to irradiation up to 30 dpa. Interestingly, formation of dislocation loops in NE SiC seems suppressed under irradiation at 700 °C to 30 dpa, which may inhibit bubble growth by eliminating biased sinks for interstitials.

This can be understood, in part, as due to a higher number of nucleation sites provided by the high-density stacking faults and grain boundaries. While sub-nm helium bubbles are not observable with certainty in the as-implanted and annealed samples, within the resolution limits of the microscope, bubbles of about 1 nm size and larger are observed following heavy-ion irradiation at 700 °C to 10 dpa. Since the implanted Au^{3+} ion peak is located far (in the substrate) from the helium implanted region, possible effects related to implanted Au ions are negligible, and only the defects created along the Au ion path will contribute to the nucleation and growth of helium bubbles. Under high-dose irradiation at 700 °C, interstitial loops should readily form in SiC [119], leaving a supersaturation of vacancies; these vacancies and the more mobile helium can interact and precipitate to promote bubble nucleation and growth. Because of the grain boundary enhanced bubble growth by providing preferential sink sites for defects and helium, the size of the helium bubbles (from 1 to 5 nm) formed at grain boundaries is significantly larger than the average helium bubble size inside the grains (from 1 to 2 nm), Moreover, bubble migration might also be enhanced along grain boundaries. The relative increase in bubble size, from sub-nm for thermal annealing to > 1 nm under irradiation, may suggest a slight irradiation-induced bubble coarsening process, as proposed by Trinkaus *et al* [120].

Because the most probable positions for helium atoms to occupy in a lattice are substitutional (helium atoms in vacancies) and interstitial sites, the dominant migration mode (including preferential position effects) depends not only on temperature, but also on the interaction with irradiation-induced defects, such as vacancies that act as traps for helium atoms to form helium–vacancy clusters. When the vacancy concentration is significantly increased by irradiation, the substitutional sites are preferred due to the strong binding of helium atoms to vacancies. For helium bubble formation, both substitutional and interstitial helium defects may be involved. The substitutional helium-vacancy complexes act either as a bubble nuclei or source of helium from de-trapping mechanisms, and the interstitial helium provides a flux of helium to nucleation sites. The migration energies for interstitial helium have been estimated for bulk SiC to be in the range from 1.1 eV [121] to 1.5 eV [122], and the de-trapping energy of helium from helium-vacancy clusters is about 3.2 eV [122]. However, the migration and de-trapping energies for interstitial defects in NE SiC are significantly decreased relative to bulk SiC [22], and similar behavior might occur for interstitial helium and vacancies. The supersaturation of vacancies near bubble nuclei and the possible migration of vacancies in NE SiC should promote the growth of bubbles under irradiation over the thermal nucleation of bubbles, leading to larger bubbles, lower bubble densities and a bimodal distribution at later growth stages. The grain boundaries can preferentially stabilize the bubble nuclei and enhance bubble growth by trapping helium atoms [123], which agrees with Chen *et al*.'s and Keng *et al*.'s observations of helium bubble aggregation in SiC [4; 89].

We observe that the average diameter of helium bubbles after high temperature Au^{3+} ions irradiation is much larger than that for the sub-nm bubbles tentatively identified in specimens processed by thermal annealing. Under the non-equilibrium irradiation environment at high temperature (700 °C), helium bubble coarsening is strongly enhanced by Au^{3+} ion irradiation. Although thermal

annealing might also enhance bubble coarsening over much longer times or at higher temperatures [124], the thermal growth of helium bubbles is not as effective as irradiation-induced growth under a constant defect production rate.

Due to the resolution limitations of the TEM measurements, the tentative number of sub-nm bubbles estimated from the TEM images is included only as a dashed line in the size distributions shown in Fig. 6-1.

6.3. Helium diffusion associated with SF confinement

A previous study [22] has shown an increase in threshold amorphization dose for NE SiC compared to single crystal SiC. The accumulation of irradiation-induced defects can be significantly reduced due to the presence of many SFs, grain boundaries and also the grain texture. Defects created from nuclear collision cascades are confined between the SFs and annihilated at grain boundaries or by recombination within the SFs. Based on DFT calculations, the presence of SFs makes interstitial defects more mobile parallel to the SFs and decreases the binding energy of interstitial-antisite defects, both of which suppress or delay defect accumulation [22; 107]. The Si interstitial annihilation at grain boundaries and the Si antisite removal phenomenon are also enhanced due to the presence of SFs, thus enabling defect migration and defect interactions in NE SiC. In our study, the ToF-ERDA results demonstrate that helium diffusion normal to the surface is negligible under irradiation at 700 °C. The increased nucleation of bubbles at grain boundaries suggests enhanced helium and defect migration parallel to the stacking faults, but not across the stacking faults (normal to the surface). Therefore, both the enhanced radiation tolerance (suppressed dislocation loop formation) and helium confinement in the NE SiC film under ion-irradiation at 700 °C to 30 dpa are attributed to the high density of SFs.

6.4. Helium bubble formation

It has been reported that helium migration can be significantly enhanced as temperature increases due to the increased mobility of defects [69; 74; 87], especially when vacancies become mobile. In the temperature range for interstitial helium migration, from 750 to 1060 °C, the helium diffusion coefficient is reported to be given by D (cm^2/s) = 1.38×10^{-10} exp{-0.91 ± 0.07 (eV/atom)/kT} [125]. Thus, increasing the temperature from 750° C to 1000 °C results in an order of magnitude increase in helium diffusivity. However, once the vacancies become mobile at high temperatures, helium release in single crystal SiC occurs, resulting in up to 95 % helium release at 1300 °C [74].

In the present study, the incident helium ions are deposited in the nano-grains and SF layers, and produce some defects within the low-energy recoil cascades. Although the implanted helium atoms can be thermally activated to migrate, it can only occur at very high temperature (above 1000 °C, [126]). At 700 °C, the diffusion coefficient is less than 4.54 x 10^{-15} cm^2/s, which is one order of magnitude less than the value at 1000 °C (i.e., 34.36 x 10^{-15} cm^2/s). At 700 °C, any residual implanted helium atoms will have limited diffusivity, resulting in no observable bubbles. It was reported by Duh *et. al.* [87] and Miro *et. al*. [118] that only a small portion of helium-vacancy pairs (vacancy trapped helium atom) can become mobile as the temperature exceeds 800 to 1100 °C. This suggests that, at the temperature of our experiments (700 °C), helium diffusion in NE SiC is limited and assumed to be dominated by interstitial diffusion.

During the high temperature heavy ion irradiation, the collision cascades provide not only kinetic energy transfer to helium atoms, whether as interstitials, in vacancies or within bubbles, but also create irradiation-induced defects. It has been suggested that the formation of gas bubbles in SiC is strongly associated with defects and dislocations [67; 107]. In the present study, the density of helium

bubbles is found to increase with irradiation dose (as shown in Table 4-2); however, the helium bubble size increases only slightly with implanted helium concentration, and is independent of irradiation dose for a given helium concentration, as shown in Table 4-1. Therefore, the migration and interaction dynamics of both defects and helium atoms are driving only nucleation processes but not growth [127]. Only a small fraction of the implanted helium atoms are participating the nucleation process.

During irradiation, both the interstitials and helium atoms are mobile at 700 °C. Thus, more helium bubbles are observed within the grains as the irradiation dose increases. Although the irradiation dose is as high as 30 dpa, the helium bubbles did not grow to any noticeable extent. On the other hand, the helium bubble density increased significantly, from 4 to 10 times, as the irradiation dose increased (i.e. see Table 4-1 and 4-2). The lack of significant bubble growth with dose up to 30 dpa suggests bubbles are undergoing continuous growth and shrinkage during the nucleation process that leads to a long incubation dose prior to the onset of bubble growth. This may be due to the high mobility of Si and C interstitials, the lack of dislocation loop formation, and the limited mobility of helium. Significant bubble growth and swelling may in fact be suppressed in this structure because of the lack of dislocation loops to provide a biased sink for interstitials.

6.5. Bubble sizes and densities

A comparison of bubble size and density from this study with literature data is summarized in Table 6-1. As reported in previous studies, hydrogen enhances bubble nucleation and inhibits bubble growth in SiC, which has been validated in comparisons of dual and triple ion beam irradiation results. At 700 °C, bubbles were found to have a smaller average size in NE SiC than in SiC composites irradiated at 800 °C, although the number densities are comparable. At 800 °C for SiC composites, as damage increases from 10 to 100 dpa, bubble growth can

Table 6-1. Summary of density and diameter of bubble of NE SiC and SiC_f/SiC composite irradiated from 10 dpa to 100 dpa at 700 °C to 1300 °C

	Conditions			Mean Size (nm)		Correspond Density (10^{-22} m^3)	
NE SiC	8000 ~ 800 He appm/	10 dpa	700 °C	1.7 ~ 2.4		0.7 ~ 0.6	
		30 dpa		1.7 ~ 2.4		5.4 ~ 2.1	
				Matrix	Fiber	Matrix	Fiber
SiC_f/ SiC comp-osite	Dual beam 1300 He appm/ *Keng *et al.* [89]	10 dpa	800 °C	1.2	-	0.85	-
	Dual beam 13000 He appm/ *Keng *et al.* [89]	100 dpa		9	5	0.26	0.45
	Dual beam 1300 He appm/ *Miwa *et al.* [128]	10 dpa	800 °C ~ 1200 °C	3.7 ~ 21.9	0 ~ 3.8	1 ~ 6	-
	Dual beam 1300 He appm/ * Taguchi *et al.* [48]		1000 °C ~ 1300 °C	4.9 ~ 23.2	-	1.61 ~ 5.92	-
	Triple beam 1300 He appm/ 400 H appm * Hasegawa *et al.* [129]		800 °C ~ 1000 °C	4.4 ~ 4.6	0 ~ 2.7	0.9 ~ 3.3	-
	Triple beam 1300 He appm/ 400 H appm * Chen *et al.* [130]		900 °C ~ 1200 °C	2.2 ~ 2.8	1.3 ~ 2.1	6.1 ~ 2.1	1.2 ~ 7.1
	Triple beam 1300 He appm/ 400 H appm * Taguchi *et al.* [48]		1000 °C ~ 1300 °C	4.6 ~ 20.9	-	2.51 ~ 7.22	-

be observed. Dramatic bubble coalescing into larger size bubbles has only been observed once the irradiation temperature exceeds 1000 °C, which can also lead to a decrease in the number density.

Normalized bubble size distributions in the NE SiC after irradiation have been determined and summarized in Fig. 6-1. Bubble sizes below 1 nm are included as a dashed line due to the limitation and uncertainty of the TEM observations. For the specimens with low helium fluence (1×10^{15} ions cm^{-2}), the density of helium bubbles increased significantly as the irradiation dose increased from 10 to 30 dpa; however, the helium bubbles exhibit similar size distributions but with decreased deviation in size with increasing dose. For the highest implanted helium concentration (1×10^{16} ions cm^{-2}), a clear transition in the bubble size distribution is observed with increasing irradiation dose. A bimodal size distribution is clearly observed for irradiation to 10 dpa, similar to that observed in Be-doped SiC irradiated with triple ion beams [131]. However, increasing the dose to 30 dpa results in a decrease in the divergence of the bubble size distribution, and the bimodal distribution transforms into a Gaussian distribution with a similar average bubble size. This may be due in part to the shrinkage of some larger bubbles with increasing dose, due to helium ejection from the bubbles by kinetic energy transfers from recoils, which is consistent with a previous study by Pawley *et al*. [132] who found that bubble growth can be inhibited by displacive irradiation in 4H SiC. Compared to the helium-implanted sample with thermal ramp alone, the present results show evidence that the bubble growth rate is indeed inhibited, which can be attributed to the displacement of helium out of the bubbles by the collision cascades from incident Au ions.

For the specimens implanted to the medium helium concentration (3×10^{15} ions cm^{-2}), the larger bubble sizes at 10 dpa disappear, and there is a similar size distribution at 20 and 30 dpa, with an average bubble size of about 1.7 nm. There

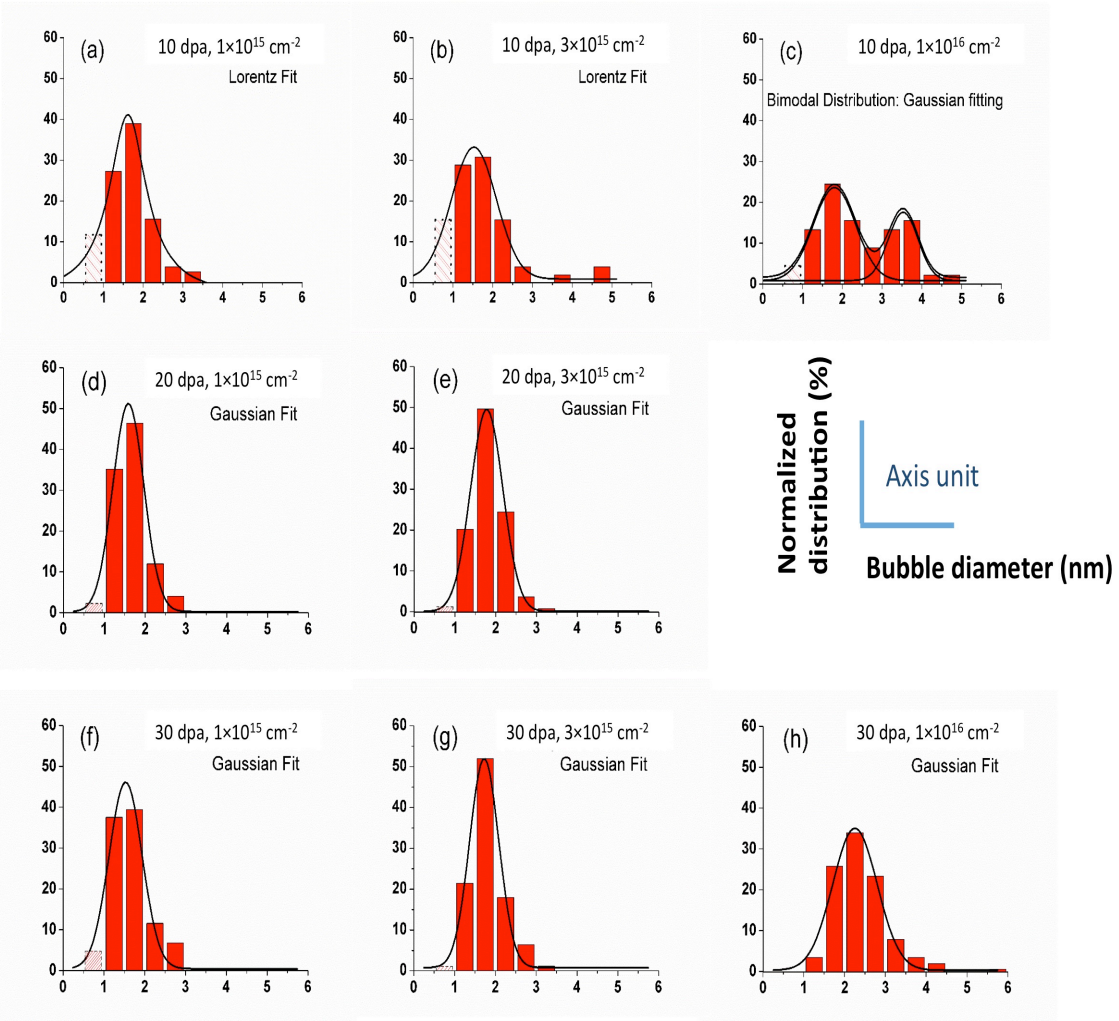

Fig. 6-1. Normalized bubble size distribution in NE SiC after irradiation from 10 to 30 dpa at 700 °C with helium fluence of 1×10^{15} cm^{-2}, 3×10^{15} cm^{-2}, and 1×10^{16} cm^{-2}.

is a consistent loss of larger bubble sizes with increasing dose for each implanted helium concentration, suggesting that an equilibrium size distribution eventually forms at higher doses.

Although the free surface and film/substrate interface can act as sinks for helium, in this study, helium bubbles with measurable size are only observed in a depth range from 270 to 390 nm from the surface, which is consistent with the helium implantation profile with the helium concentration peak at 320 nm. This suggests that helium atom diffusion primarily occurs two-dimensionally and over a short range in the NE SiC under the current irradiation temperature. The SFs exhibit significant radiation tolerance by retaining their self-layered interface structure after heavy ion irradiation to 30 dpa at 700 °C. The confinement of the helium in the NE SiC film under ion-irradiation to 30 dpa may be attributed to the high density SFs, which modified the migration pathways for the helium atoms into 2D-like interlayer diffusion.

6.6. Microstructural evolution under *in-situ* irradiation

For *in-situ* radiation at low temperature (350 °C), due to the low mobility for defect migration, no significant bubble or microstructure evolution can be observed, even after a damage dose of 20 dpa, which is similar to the results from low dose irradiation at 800 °C. However, fort higher irradiation doses at 800 °C, instead of triggering the growth of helium bubble, Kr ion irradiation actually resulted in a decrease of bubble size and number density. Because helium re-distribution within the specimen can be triggered under irradiation, some of the helium atoms can be trapped into pre-existed bubbles and result in a small amount of bubble growth. However, since the free surfaces act as strong sinks for defects and helium, the migration of helium to the surfaces dominates over

nucleation and growth, resulting in helium loss from the TEM specimen during irradiation.

The significant decrease of bubble size occurred at the second stage, as the irradiation dose exceeded 10 dpa, which provided sufficient displacement events to ballistic knock helium atoms out of the bubbles. Due to the enhanced two-dimensional defect migration and helium confinement by the SF layers in NE SiC, helium and defect diffusion to grain boundaries and surfaces is more probably than re-trapping into bubbles. As a result, the helium migrates preferentially to the free surfaces of the TEM specimen, leading to a significant helium release and bubble shrinkage as the irradiation dose exceeds 10 dpa.

Additional supporting evidence for the impeded defect migration by SFs is that bubble coalescence was not observed. Birtcher *et al.* [133] had previously demonstrated that during *in-situ* heavy ion irradiation, coalescence of two or more helium bubbles with close proximity produced larger size bubbles within irregular shapes in Al. It was also shown that due to the coalescence process, bubble growth (30 to 50 %) initiated at the beginning, then followed by a decrease in size with a linear shrinkage rate due to the sputtering and helium resolution to the matrix. However, none of the above phenomenon was observed in NE SiC during *in-situ* irradiation. Hence, helium migration and resolution into the SiC were hindered due to effects of SF layers. As a result, microstructural evolution in NE SiC is not sensitive to irradiation at low damage level.

On-the-other-hand, because the defect migration in the NE SiC is strongly related to the existence of SFs, the two-dimensional migration mechanism could no longer remain if the SF structure is not stable after irradiation. From the results of TEM bright field images and diffraction patterns, as shown in Fig 4-17 and 4-18, with a dose higher than 15 dpa, the density of SF layers decreased dramatically and some extra diffraction spots appear as the dose increases.

Those new diffraction spots, as marked with white arrows, indicate that the original SF planes have broken into planes with new orientations. Without the SF structure, the efficiency of defect confinement goes down, suggesting that this two-dimensional defect migration will transform into a three-dimensional, random diffusion under irradiation. In this temperature region, it was previously reported that the helium migration in SiC is dominant by interstitial migration [87; 118]. Since the interstitials can randomly diffuse in all directions in the specimen without the SFs confinement, the possibility for helium diffusion toward surfaces should decrease. Thus, it may reduce the helium release rate from the specimen.

Although the damage level for eliminating all SFs in NE SiC is still unknown, the critical dose of structural stability under irradiation can be acquired from *in-situ* observation. The nano-layered SF structure is radiation tolerant up to 15 dpa at 800 °C, as shown in Fig. 4-13.

6.7. Helium density and energy shift

In the EELS measurements, the linear relationship between energy shift of helium K edge and helium density are in good agreement with the literature data from both ceramics and metals [2; 40; 93]. Our results indicate that the EELS approach can be used to measure the helium distribution and gas bubble pressure in nano-scale defects in the NE SiC for nuclear application after low dose helium irradiation.

From results calculated in Ch 5, the atomic percentages of helium in bubbles are about 1 % for irradiation at 700 °C. Different from the result under 1000 °C irradiation, most of the incident helium atoms in the samples irradiated at 700 °C are not contained in the helium bubbles. Compared with the density of liquid helium, the density of helium in the bubbles found in NE SiC is consistent with a

solid or liquid phase. Above a certain critical size, the gas bubble can be stabilized and it can act as a sink for vacancies. With the absorption of vacancies, the bubbles can become voids. However, the vacancy migrations only occur under irradiation or at elevated temperature. Compared with the results from high temperature irradiation, as shown in Table 5-1, it was demonstrated that the effect of temperature is a key parameter for the helium migration and bubble formation. The percentage of helium atoms trapping in bubbles is strongly correlated with irradiated temperature.

Chapter 7. Conclusion

In this work, defect production and helium gas bubble formation are studied in both single crystal 3C SiC and nano-engineered (NE) SiC. The crystalline structure of the 3C SiC single crystal is retained after 65 keV helium implantation at 277 °C and 10 dpa Au^{3+} irradiation at 700 °C. Visible planar defects form in the helium implanted single crystal SiC after 700 °C annealing. However, no cavities are observed in single crystal 3C SiC following Au ion irradiation at 700 °C.

On-the-other-hand, helium migration perpendicular to the stacking fault direction [111] is inhibited in the NE SiC, as demonstrated from the ToF-ERDA measurement. As a result and in contrast to the behavior in single crystals, helium bubble formation is observed in a well-defined depth region around the helium concentration peak after Au^{3+} ion irradiation to doses from 10 to 30 dpa. This subsequent irradiation of the helium implanted samples with Au ions revealed preferential formation of bubbles at grain boundaries, which indicates that helium migration does occur two-dimensionally between stacking fault layers. The preferential formation of bubbles along grain boundaries may result in degradation of strength in the NE SiC.

A long bubble nucleation period with increasing dose is observed, where the bubble size remains in dynamic equilibrium and below the critical bubble size for growth, resulting in a large incubation dose. Significant bubble growth and swelling may be inhibited by the suppression of dislocation loop formation in the NE SiC. The main features of the microstructures can be understood in terms of radiation-induced defects and helium migration associated with SFs confinement in this temperature region. Compared with the results from high temperature irradiation, helium atoms exhibit a lower mobility 700 °C. According to EELS measurement, it can be estimated that about 1 at. % of the implanted helium

atoms are trapped into bubbles, suggesting that helium bubbles are still undergoing a long incubation period in this temperature region. The microstructural observations also reveal that the nano-layered SF structure in the NE SiC is highly radiation tolerant and stable under irradiation to a dose of 30 dpa at 700 °C.

During the *in-situ* Kr irradiation, significant bubble shrinkage and rare bubble growth are observed, which indicates that irradiation induced redistribution of helium atoms takes place in the thin TEM specimen. However, because of the ballistic dissolution of bubbles and presence of nearby free surfaces in the TEM sample, bubble shrinkage and helium loss are dominant under these irradiation conditions. It is revealed that the nano-layered SF structure in the NE SiC is radiation tolerant at least up to 15 dpa at 800 °C under this *in-situ* irradiation conditions. The stability under bulk irradiation has not yet been determined.

ACKNOWLEDGEMENTS

This work was supported by the DOE Office of Nuclear Energy, Nuclear Energy University Programs.

REFERENCES

[1] P. Liu, PhD. Dissertation (2014), " Atomic Structure of the Vicinal Interface between Silicon Carbide and Silicon Dioxide " (2014). University of Tennessee.
[2] A.A. Lucas, J. P. Vigneron, S. E. Donnelly, J. C. Rife, PHYSCAL REVIEW B 28 (1983) 2485-2496.
[3] R.L. Mills, D. H. Liebenberg, J. C. Bronson, PHYSICAL REVIEW B 21 (1980) 5137-5148.
[4] K.F. Chen, C. H. Chen, Z. H. Zeng, F. R. Chen and J. J. Kai, Progress in Nuclear Energy 57 (2012) 46-51.
[5] http://physicsworld.com/cws/article/news/2014/feb/12/laser-fusion-passes-milestone.
[6] L. Torrisi, Molecules 19 (2014) 17052-17065.
[7] http://www.sunist.org/Shared documents/SUNIST Lab Ceremony/00 introduction to ST/Fusion, Tokamak and Spherical Tokamak/Conditions for Fusion.htm.
[8] J.J. Berzelius, Ann. Phys., Lpz. 1 (1824) 169-230.
[9] F.H. Moissan, Comptes rendus 139 (1904) 773–786.
[10] G. Brezeanu, Silicon carbide (SiC): a short history. an analytical approach for SiC power device design, 2005, 345-348 vol. 2.
[11] Wikipedia.
[12] L.L. Snead, R. H. Jones, A. Kohyama, P. Fenici Journal of Nuclear Materials 233-237 (1996) 26-36.
[13] Y.M. Tairov, V. F. Tsvetkov, (1988).
[14] M.V. Kovalenko, M. Scheele, Dmitri V. Talapin, Science 324 (2009) 1417-1420.
[15] D.J. Norris, A. L. Efros, S. C. Erwin, Science 319 (2008).
[16] N. Swaminathan, Paul J. Kamenski, Dane Morgan, Izabela Szlufarska, Acta Materialia 58 (2010) 2843–2853.
[17] I. Szlufarska, A. Nakano, P. A. Vashishta, Science 309 (2005) 911-915.
[18] Y. Zhang, W. Jiang, C. Wang, F. Namavar, P. D. Edmondson, Z. Zhu, F. Gao, J. Lian, W J. Weber, Physical Review B 82 (2010) 184105.
[19] Y. Zhang, P D. Edmondson, T. Varga, S. Moll, F. Namavar, C. Lan, W. J. Weber, Physical Chemistry Chemical Physics 13 (2011) 11946–11950.
[20] Y. Zhang, M. Ishimaru, T. Varga, T. Oda, C. Hardiman, H. Xue, Y. Katoh, S. Shannone, W. J. Weber, Physical Chemistry Chemical Physics 14 (2012) 13429–13436.
[21] M. Ishimaru, Y. Zhang, S. Shannon, W. J. Weber, Applied Physics Letters 103 (2013) 033104.
[22] L. Jamison, M.-J. Zheng, S. Shannon, T. Allen, D. Morgan, I. Szlufarska, Journal of Nuclear Materials 445 (2014) 181-189.
[23] X.-M. Bai, A. F. Voter, R. G. Hoagland, M. Nastasi, B. P. Uberuaga, Science 327 (2010) 1631-1634.
[24] J.F. Ziegler, M. D. Ziegler, J. P. Biersack Nuclear Instruments and Methods in Physics Research B 268 (2010) 1818-1823.
[25] W. Jiang, Y. Zhang, W. J. Weber, Physical Review B 70 (2004) 165208.

[26] Y. Zhang, W. J. Weber, W. Jiang, C. M. Wang, V. Shutthanandan, A. Hallén, Journal of Applied Physics 95 (2004) 4012-4018.
[27] Y. Zhang, M. L. Crespillo, H. Xue, K. Jin, C. H. Chen, C. L. Fontana, J. T. Graham, W. J. Weber, Nucl. Instrum. and Methods in Physics Research B 338 (2014) 19–30.
[28] R. Devanathan, W. J. Weber, F. Gao, Journal of Applied Physics 90 (2001) 2303.
[29] Thermionics, Thermionics Northwast Inc., 2013.
[30] L.C. Feldman, J. W. Mayer, S. T. Picraux, , Materials Analysis by Ion Channeling, Academic Press 1982.
[31] L.C. Feldman, J. W. Mayer, Fundamentals of Surface and Thin Film Analysis, North-Holland, 1986.
[32] J. Jensen, G. Possnert, Y. Zhang, Journal of Physics: Conference Series 100 (2008) 012041.
[33] Z. Company, http://www.zeiss.com/microscopy/en_de/products/fib-sem-instruments/auriga.html - introduction.
[34] M.L. Jenkins, M. A. Kirk., (2000) 129-135.
[35] M. Rühle, M. Wilkens. , Crystal Lattice Defects (1975) 129-140.
[36] G. Duscher. *Quantifit*. Available from: http://web.utk.edu/~gduscher/Quantifit/index.html.
[37] G. Duscher, M. E. Hmielewski, J. D. O. Oduor, Microscopy and Microanalysis 15 (2009) 446-447.
[38] R.F. Egerton, Electron Energy-Loss Spectroscopy in the Electron Microscope, 1996.
[39] S. Fréchard, M. Walls, M. Kociak, J. P. Chevalier, J. Henry, D. Gorse, Journal of Nuclear Materials 393 (2009) 102–107.
[40] C.A. Walsh, J. Yuan, L. M. Brown, Philosophical Magazine A 80 (2000) 1507-1543.
[41] R.C. Birtcher, M. A. Kirk, K. Furuya, G. R. Lumpkin, M-O. Ruault, Journal of Materials Research 20 (2005) 1654-1683.
[42] J.A. Hinks, Nuclear Instruments and Methods in Physics Research B 267 (2009) 3652–3662.
[43] E.I. Moses, R. N. Boyd, B. A. Remington, C. J. Keane, R. Al-Ayat, Physics of Plasmas 16 (2009) 041006
[44] H. Holtkamp, Fusion Engineering and Design 84 (2009) 98–105.
[45] K. Ehrlich, E. E. Bloom, T. Kondo, Journal of Nuclear Materials 283-287 (2000) 79-88.
[46] H. Kishimoto, Y. Katoh, A. Kohyama, Journal of Nuclear Materials 307–311 (2002) 1130–1134.
[47] L.K. Mansur, A. F. Rowcliffe, R. K. Nanstad, S. J. Zinkle, W. R. Corwin, R. E. Stoller, Journal of Nuclear Materials 329–333 (2004) 166–172.
[48] T. Taguchi, N. Igawa, S. Miwa, E. Wakai, S. Jitsukawa, L. L. Snead, A. Hasegawa, Journal of Nuclear Materials 335 (2004) 508–514.
[49] H.L. Heinisch, L. R. Greenwood, W. J. Weber, R. E. Williford, Journal of Nuclear Materials 327 (2004) 175-181.

[50] Y. Katoh, T. Nozawa, L. L. Snead, K. Ozawaa, H. Tanigawa, Journal of Nuclear Materials 417 (2011) 400-405.
[51] M. Toulemonde, W. J. Weber, G. Li, V. Shutthanandan, P. Kluth, T. Yang, Y. Wang, Y. Zhang, Physical Review B 83 (2011) 054106.
[52] J. Zhang, M. Lang, R. C. Ewing, R. Devanathan, W. J. Weber, M. Toulemonde, Journal of Materials Research 25 (2010) 1344-1351.
[53] A. Debelle, M. Backman, L. Thome´, W. J. Weber, M. Toulemonde, S. Mylonas, A. Boulle, O. H. Pakarinen, N. Juslin, F. Djurabekova, K. Nordlund, F. Garrido, D. Chaussende, Physical Review B 86 (2012) 100102.
[54] M. Ishimaru, I-T Bae, Y. Hirotsu, Physical Review B 68 (2003) 144102.
[55] X. Yuan, L. W. Hobbs, Nuclear Instruments and Methods in Physics Research B 191 (2002) 74–82.
[56] Y. Zhang, W. J. Weber, W. Jiang, A. Hallen, G. Possnert, Nuclear Instruments and Methods in Physics Research B 195 (2002) 320–328.
[57] Y. Katoh, L. L. Snead, I. Szlufarska, W. J. Weber, Current Opinion in Solid State and Materials Science 16 (2012) 143–152.
[58] E. Wendler, A. Heft, W. Wesch, Nuclear Instruments and Methods in Physics Research B 141 (1998) 105-117.
[59] M. Ishimaru, I-T Bae, Y Hirotsu, S. Matsumura, K. E. Sickafus, Physical Review Letters 89 (2002) 055502.
[60] B. Azadegan, S. B. Dabagov, W. Wagner, Journal of Physics: Conference Series 357 (2012) 012027.
[61] S.J. Zinkle, Nuclear Instruments and Methods in Physics Research B 286 (2012) 4-19.
[62] E. Oliviero, M. F. Beaufort, J. F. Barbot, Journal of Applied Physics 93 (2003) 231-238.
[63] P. Jung, H. Klein, J. Chen, Journal of Nuclear Materials 283-287 (2000) 806–810.
[64] K. Hojou, S. Furuno, K. N. Kushita, H. Otsu, K. Izui Nuclear Instruments and Methods in Physics Research B 91 (1994) 534-539.
[65] S. Kondo, T. Hinoki, A. Kohyama, Materials Transactions 46 (2005) 1388-1392.
[66] J.F. Barbot, S. Leclerc, M. -L. David, E. Oliviero, R. Montsouka, F. Pailloux, D. Eyidi, M. -F. Denanot, M. -F. Beaufort, A. Decle´my, V. Audurier, C. Tromas, Physical Status Solidi A 206 (2009) 1916–1923.
[67] C.H. Zhang, S. E. Donnelly, V. M. Vishnyakov, J. H. Evans, T. Shibayama, Y. M. Sun, Nuclear Instruments and Methods in Physics Research Section B 218 (2004) 53-60.
[68] E. Oliviero, M. F. Beaufort, F. Pailloux, J. F. Barbot, Nuclear Instruments and Methods in Physics Research B 218 (2004) 391–395.
[69] E. Oliviero, C. Tromas, F. Pailloux, A. Decle´my, M.F. Beaufort, C. Blanchard, J.F. Barbot, Materials Science and Engineering B 102 (2003) 289-292.
[70] E. Oliviero, M. L. David, M. F. Beaufort, Journal of Applied Physics 91 (2002) 1179-1186.

[71] M.F. Beaufort, F. Pailloux, A. Decle´my, and J. F. Barbot, Journal of Applied Physics 94 (2003) 7116-7120.
[72] C.H. Zhang, S. E. Donnelly, V. M. Vishnyakov, J. H. Evans, Journal of Applied Physics 94 (2003) 6017-6022.
[73] F. Linez, F. Garrido, H. Erramli, T. Sauvage, B. Courtois, P. Desgardin, M.-F. Barthe Journal of Nuclear Materials 459 (2015) 62–69.
[74] L. Vincent, T. Sauvage, G. Carlot, P. Garcia, G. Martin, M. F. Barthe, P. Desgardin, Vacuum 83 (2009) S36-S39.
[75] T. Sauvage, G. Carlot, G. Martin, L. Vincent, P. Garcia, M. F. Barthe,, P.D. A. Gentils, Nuclear Instruments and Methods in Physics Research B 257 (2007) 231–235.
[76] J. Chen, P. Jung, H. Trinkaus, Physical Review Letters 82 (1999) 2709-2712.
[77] K. Sasaki, T. Yano, T. Maruyama, T. Iski, Journal of Nuclear Materials 179-181 (1991) 407-410.
[78] W.R. Allen, Jurnal of Nuclear Materials 210 (1994) 318-323.
[79] K. Hojou, S. Furuno, K. N. Kushita, H. Otsu, Y. Furuya, K. Izui Nuclear Instruments and Methods in Physics Research B 116 (1996) 382-388.
[80] J. Chen, P. Jung, H. Trinkaus, Physical Review B 61 (2000) 12923.
[81] W. Jiang, W. J. Weber, C. M. Wang. Y. Zhang, Materials Research Society 17 (2002) 271-274.
[82] K. Hojou, S. Furuno, K.N. Kushita, N. Sasajima, K. Izui, Nuclear Instruments and Methods in Physics Research B 141 (1998) 148-153.
[83] K. Hojou, K. Izui, Journal of Nuclear Materials 160 (1988) 147-152.
[84] K. Hojou, K. Izui, Journal of Nuclear Materials 133-134 (1985) 709-713.
[85] H.W. Scholz, A. J. Frias Rebelo, D. G. Rickerby, P. Krogul, W. E. Lee, J. H. Evans, P. Fenici, Journal of Nuclear Materials 258-263 (1998) 1572-1576.
[86] L.L. Snead, M. C. Osborne, R. A. Lowden, J. Strizak, R.J. Shinavski, K. L. More, W. S. Eatherly, J. Bailey, A. M. Williams, Journal of Nuclear Materials 253 (1998) 20-30.
[87] T.S. Duh, K. M. Yin, J. Y. Yan, P. C. Fang, C. W. Chen, J. J. Kai, F. R. Chen, Y. Katoh, A. Kohyama, Journal of Nuclear Materials 329-333 (2004) 518-523.
[88] B. Riccardi, L. Giancarli, A. Hasegawa, Y. Katoh, A. Kohyama, R. H. Jones, L. L. Snead, Journal of Nuclear Materials 329–333 Part A (2004) 56–65.
[89] H.T. Keng, S. W. Li, S. W. Wu, J. J. Kai, F. R. Chen, Y. Katoh, A. Kohyama, Journal of Nuclear Materials 367-370 (2007) 753-757.
[90] A. Hasegawa, M. Saito, S. Nogami, K. Abe, R. H. Jones, H. Takahashi, Journal of Nuclear Materials 264 (1999) 355-358.
[91] H. Kishimoto, Y. Katoh, A. Kohyama, Journal of Nuclear Materials 307–311 (2002) 1130–1134.
[92] S. Nogami, A. Hasegawa, K. Abe, T. Taguchi, R. Yamada, Journal of Nuclear Materials 283-287 (2000) 268-272.
[93] T. Taguchi, E. Wakai, N. Igawa, S. Nogami, L. L. Snead, A. Hasegawa, S. Jitsukawa, Journal of Nuclear Materials 307–311 (2002) 1135–1140.

[94] A. Hasegawa, B. M. Oliver, S. Nogami, K. Abe, R. H. Jones, Journal of Nuclear Materials 283-287 (2000) 811-815.
[95] D.M. Follstaedt, S. M. Myers, C. A. Petersen, and J. W. Medernach, J.Electron. Mater. 25, 157 1996, 25 (1996) 157-163.
[96] T. Taguchi, E. Wakai, N. Igawa, S. Nogami, L. L. Snead, A. Hasegawa, S. Jitsukawa, Journal of Nuclear Materials 307-311 (2002) 1135-1140.
[97] H. Fan, R. Li, D. Yang, Y. Wu, J. Niu, Q. Yang, J. Zhao, D. Liu, Journal of Nuclear Materials 441 (2013) 54–58.
[98] A.R. Raffray, R. Jones, G. Aiello, M. Billone, L. Giancarli, H. Golfier, A. Hasegawa, Y. Katoh, A. Kohyama, S. Nishio, B. Riccardi, M. S. Tillack, Fusion Engineering and Design 55 (2001) 55–95.
[99] S.A. Maloy, M. R. James, W. R. Johnson, T. S. Byun, K. Farrell, M. B. Toloczko, Journal of Nuclear Materials 318 (2003) 283–291.
[100] S. Leclerc, A. Declémy, M. F. Beaufort, C. Tromas, J. F. Barbot, Journal of Applied Physics 98 (2005) 113506.
[101] Y. Katoh, H. Kishimoto, A. Kohyama, Journal of Nuclear Materials 307-311 (2002) 1221–1226.
[102] H. Kurishita, S. Kobayashi, K. Nakai, T. Ogawa, A. Hasegawa, K. Abe, H. Arakawa, S. Matsuo, T. Takida, K. Takebe, M. Kawai, N. Yoshid, Journal of Nuclear Materials 377 (2008) 34–40.
[103] S.-C.T. C. -Y. Ho, H. -T. Lin, F. -R. Chen, J. -J. Kai, Journal of Nuclear Materials 443 (2013) 1-7.
[104] M.-J.Z. L. Jamison, S. Shannon, T. Allen, D. Morgan, I. Szlufarska, Journal of Nuclear Materials 445 (2014) 181-189.
[105] R.H. Jones, L. Giancarli, A. Hasegawa, Y. Katoh, A. Kohyama, B. Riccardi, L. L Snead, W. J Weber, Journal of Nuclear Materials 307–311, Part 2 (2002) 1057-1072.
[106] T. Nozawa, Y. Katoh, L. L. Snead, Journal of Nuclear Materials 384 (2009) 195-211.
[107] P. Pirouz, Solid State Phenomena 56 (1997).
[108] F. Schiettekatte, M. Chicoine, S. Gujrathi, P. Wei, K. Oxorn, Nuclear Instruments and Methods in Physics Research B 219–220 (2004) 125–129.
[109] C.H. Chen, Y. Zhang, E. Fu, Y. Wang, M. L. Crespillo, C. Liu, S. C. Shannon, W.J. Weber, Journal of Nuclear Materials 453 (2014) 280–286.
[110] S. Kondo, K. H. Park, Y. Katoh, A. Kohyama, Fusion Science and Technology 44 (2003) 181-185.
[111] D. Taverna, M. Kociak, O. Ste´phan, A. Fabre, E. Finot, B. De´camps, C. Colliex, PHYSICAL REVIEW LETTERS 100 (2008) 035301.
[112] P.R. Taylor, CHEMICAL PHYSICS LETTERS 121 (1985).
[113] J.C. Rife, S. E. Donnelly, A. A. Lucas, J. M. Gilles, J. J. Ritsko, PHYSICAL REVIEW LETTERS 46 (1981) 1220-1223.
[114] H.G. Kuhn, Atomic Spectra Longmans, London: , 1962.
[115] C.M. Surko, G. J. Dick, F. Reif, W. C. Walker, PHYSICAL REVIEW LETTERS 23 (1969) 842-846.
[116] S.E. Donnelly, A. A. Lucas, J. P. Vigneron, J. C. Rife, 78 (1983) 337-347.

[117] S.E. Donnelly, J. C. Rife, J. M. Gilles, A.A. Lucas, Journal of Nuclear Materials 93-94 (1980) 767-772.
[118] S. Miro, J. M. Costantini, J. Haussy , L. Beck , S. Vaubaillon , S. Pellegrino , C. Meis , J. J. Grob, Y. Zhang, W. J. Weber, Journal of Nuclear Materials 415 (2011) 5-12.
[119] S. Kondo, T. Hinoki, A. Kohyama, Materials Transactions Vol. 46 (2005) 1388-1392.
[120] H. Trinkaus, B. N. Singh, Journal of Nuclear Materials 323 (2003) 229-242.
[121] D. Jung, Journal of Nuclear Materials 191-194 (1992) 377-381.
[122] E. Oliviero, A. van Veen, A. V. Fedorov, M. F. Beaufort, J. F. Barbot, Nuclear Instruments and Methods in Physics Research B 186 (2002) 223-228.
[123] L. Vincent, T. Sauvage, G. Carlot, P. Garcia, G. Martin, M.F. Barthe, P. Desgardin, Vacuum 83 (2009) 536-539.
[124] C.H. Zhang, S. E. Donnelly, V. M. Vishnyakov, and J. H. Evans Journal of Applied Physics 94 (2003) 6017-6022.
[125] Y. Pramono, K. Sasaki, T. Yano, Journal of Nuclear Science and Technology 41 (2004) 751–755.
[126] J.F. Barbot, M. F. Beaufort, M. Texier, C. Tromas, Journal of Nuclear Materials 413 (2011) 162–165.
[127] W.J. Weber, D. M. Duffy, L. Thomé, Y. Zhang, Current Opinion in Solid State & Materials Science (2014).
[128] S. Miwa, A. Hasegawa, T. Taguchi, Naoki Igawa, K. Abe, Materials Transactions 46 (2005) 536-542.
[129] A. Hasegawa, S. Miwa, S. Nogami, A. Taniguchi, T. Taguchi, K. Abe, Journal of Nuclear Materials 329–333 (2004) 582–586.
[130] C.H. Chen, J. J. Kai, F. R. Chen, Y. Katoh, Advances in Science and Technology 73 (2010) 27-35.
[131] T. Taguchi, N. Igawa, E. Wakai, S. Jitsukawa, L. L. Snead, A. Hasegawa, Nuclear Instruments and Methods in Physics Research B 256 (2007) 669–674.
[132] C.J. Pawley, M. F. Beaufort, E. Oliviero, J. A. Hinks, J. F. Barbot, S. E. Donnelly, Journal of Physics: Conference Series 371 (2012) 012052.
[133] R.C. Birtcher, S. E. Donnelly, C. Templier, Physical Review B 50 (1994) 764-769.

VITA

Chien-Hung (Curtis) Chen was born in Taipei, Taiwan, where he finished his primary and secondary education. Chien-Hung earned his B.S. and M.S. in the Department of Engineering and System Science from the National Tsing-Hua University (NTHU), Taiwan in 2006 and 2008, respectively. From 2010 to 2011, Chien-Hung was a research assistant at the TEM Analysis Laboratory in NTHU, where he studied crystal defects and radiation effects in nuclear materials.

After that, Chien-Hung joined the Department of Materials Science and Engineering at the University of Tennessee, Knoxville to conducted research on radiation effects in ceramics using both electron microscopy analysis and ion beam analysis techniques. Besides devoting himself to microscopy analysis, Chien-Hung was also an operator for the Tandem accelerator system in the Ion Beam Materials Laboratory at the UT, where he provided technical assistance in fundamental research on ion-solid interactions.

Supervised by Prof. William J. Weber and Prof. Yanwen Zhang, his dissertation research focused the nano-structure enhanced defect migration and bubble formation in ion-irradiated SiC.